Ben-Gurion University of the Negev

The Faculty of Natural Sciences

The Department of Physics

Electric Feedback Cooling of Nanoparticles in a Paul Trap

Thesis submitted in partial fulfillment of the requirements for the

Master of Sciences degree

Ben Shultz

Under the supervision of: **Prof. Ron Folman**

March 2026

Ben-Gurion University of the Negev

The Faculty of Natural Sciences

The Department of Physics

Electric Feedback Cooling of Nanoparticles in a Paul Trap

Thesis submitted in partial fulfillment of the requirements for the Master of Sciences degree

Ben Shultz

Under the supervision of: **Prof. Ron Folman**

Signature of student: ____________________ Date: 25.03.2026

Signature of supervisor: ____________________ Date: 25.3.2026

Signature of chairperson of the committee for graduate studies: ____________________ Date: ____________

March 2026

Electric Feedback Cooling of Nanoparticles in a Paul Trap

Ben Shultz

Master of Sciences Thesis

Ben-Gurion University of the Negev

2026

Abstract

This thesis presents the development and implementation of an electric feedback cooling system for levitated nanoparticles in a Paul trap, with the aim of advancing precision control in levitodynamics experiments. A custom-designed end-cap Paul trap was employed to stably confine charged nanoparticles and electric feedback was used to slow their motion and cool them. Optical detection of the particle's translations in real-time is realized by a homodyne interference scheme of the forward scattered light and heterodyne detection of back scattered light. Two active feedback techniques were investigated: velocity damping and parametric. Both methods were implemented on a Red Pitaya (RP) FPGA-based platform to meet the stringent requirements for low-latency feedback. The cooling results shown in this work were achieved by both velocity damping and parametric techniques. It is also important to point out that while the research and implementation of the velocity damping cooling were done by me, the best cooling results were done by my lab colleagues while I was away on reserve duty. As a result of our work, we recently posted a preprint in the archive [1].

The experimental system described in this thesis is the result of the work of two PhD students, a postdoc, and myself. I participated in designing and building the trapping system and in assembling the vacuum system, but the main focus of my work was on the cooling system and the micromotion minimization procedure.

Acknowledgments

This thesis benefited from the support, guidance, and collaboration of many individuals, to whom I am deeply grateful.

I would like to begin by acknowledging Prof. Ron Folman for his consistent mentorship and thoughtful guidance throughout the course of my research. His academic leadership and insightful feedback were essential to the development and results of this work.

I am especially thankful to Dr. David Grosswasser, whose close supervision and technical expertise played a vital role in the execution of the experimental components of this project. His availability, patience, and practical advice were central to overcoming many challenges during this process.

Dr. Menachem Givon provided key administrative and facilitated financial support throughout my studies. His assistance in navigating institutional requirements allowed me to focus on my research. I am also grateful to Dr. Or Dobkowski for his theoretical input and for his important role during the final phase of writing this thesis. His contributions helped clarify key aspects of the research and facilitated its timely completion.

The successful operation of the experimental setup depended heavily on the contributions of several team members. I thank Zina Binshtok for her reliable support with the electrical systems and readiness to assist whenever needed. Yaniv Bar-Haim made substantial contributions involving many technical domains, from joint apparatus construction to independent system development, offering both practical expertise and ongoing advice. Bar Shaybet, our FPGA engineer, played a crucial role in implementing the detection and cooling algorithms on hardware.

I also wish to thank Sergey Popov for his precise work in designing and assembling the electrospray mechanism. His attention to detail directly supported the reliability of the system.

I appreciate the collaboration with the nano-diamond research team, whose involvement was very important to this project. I would also like to acknowledge my MSc colleague Omer Feldman, who provided critical day-to-day support and collaboration throughout the program, and Maria Muretova for her contributions and engagement throughout the project. I am further grateful to Petr Skakunenko for his technical input, particularly regarding the design and modeling of the Paul trap, which enriched the experimental planning.

The lab environment itself benefited greatly from the participation of many other colleagues. I thank Naor Levi, Barak Trok, Ofir Yitzhak, and Itamar Haskel for contributing to a productive and collegial atmosphere. I also acknowledge Dima Kapusta, who introduced me to the experimental system and provided essential background that helped me get started.

Lastly, I am deeply thankful to my family. My parents, Barry and Tamar, have been a constant source of encouragement and support throughout this academic journey. Most of all, I wish to thank my partner, Ester, whose understanding and support made this endeavor sustainable.

Contents

1 Introduction

In the field of quantum optics, there are exciting possibilities for experiments to test the boundaries of quantum mechanics on mesoscopic systems that can also exhibit effects from the second pillar of modern physics, namely, general relativity, and more specifically, gravity. This allows one to test not only quantum mechanics in new regimes, but also the interface between quantum and gravity. Spin-based matter-wave interferometry [2] is a powerful technique for such investigations [3]. The state of the art for putting a large mass in a verifiable spatial superposition stands at a cluster of about 7000 atoms [4]. In this project, we aim to develop the technology to go far beyond that to approximately $10^7 - 10^{11}$ atoms. Rather than the method used to obtain the state of the art above (a particle beam traversing a near-field spatial interferometer), we aim to start with a trapped particle for which we can cool the external degrees of freedom, and then use the Stern-Gerlach effect together with an embedded spin to coherently split the particle [2, 3, 5].

The first challenge that arises in attempting to realize such experiments is to trap an isolated (levitated) particle with a mass that is small enough to observe its quantum behavior and also large enough to observe its gravitational behavior. There are several different trapping techniques, each with its own strengths and weaknesses [6]. These include optical tweezers [7], magneto-gravitational traps [8] and ion traps [9]. Trapping a nanoparticle is only the initial step towards a matter-wave interferometry experiment. Cooling the particles' Center-of-Mass (CoM) motion is necessary to realize a macroscopic coherent quantum system. Levitated nanoparticle cooling methods are generally divided into two families: passive and active. Passive methods can be employed with particles in a dipole trap inside an optical cavity [10]. Active methods include neutral particles trapped by optical tweezers and charged particles in an ion trap, which is the subject of this thesis. Active cooling methods are divided into parametric and velocity damping schemes. Both are based on detecting the motion of the particle in the trap and applying a restoring force in real-time to counter the particle's motion. In parametric cooling, this is achieved by modulating the trapping potential, while in velocity damping, an additional cooling force proportional to the particle velocity is added to the system. For example, parametric cooling is often used to cool optically trapped particles in a dipole trap [11]. In this case, the trap frequency is a function of the trapping laser power, which can be modulated proportionally to the magnitude of the particle velocity [12]. For a charged particle in an ion trap, parametric cooling is realized by modulating the voltage of the trapping electrodes. Velocity damping cooling requires an external force to counter the particle's motion. For a charged particle in an ion trap, an electric force is realized by applying voltage on nearby electrodes [13]. Magnetic forces can also be used to cool an ion in a magneto-gravitational trap[14]. In both methods, the cooling feedback is dependent on the dynamic state of the particle. Therefore, real-time accurate measurements of the particle's position are crucial. The application of an iterative Kalman filtering algorithm enables improvement in the determination of the particle's position using not only the measurements but also predictions of the particle's position based on the equations of motion for the particle in the trap, thus enabling higher quality feedback and an increased cooling rate. Magrini *et al* [13] demonstrated ground state cooling using this method.

2 Background

2.1 Paul trap

2.1.1 Introduction to ion trapping

According to Earnshaw's theorem, a point charge cannot be maintained in a stable stationary equilibrium configuration solely by an arbitrary static electric field. Therefore, to trap an ion by interaction with an electric field would require it to be dynamic, as demonstrated by the German physicist Wolfgang Paul [15]. Using hyperbolic electrodes connected to an alternating electric potential at radio-frequency (RF), he was able to trap numerous ions with different masses.

An illustration of an ideal Paul trap with infinite hyperboloid electrodes is presented in Fig. 1:

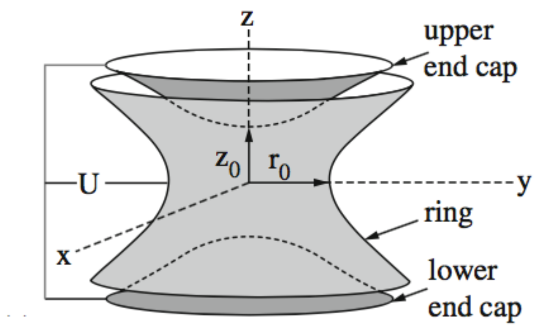

Figure 1: Depiction of a hyperboloid Paul trap taken from [16]. An oscillating electric potential with a static offset of the form $U = U_0 + V_0 cos\Omega t$ is applied between the pair of end-cap electrodes to the ring. An electric potential, modulated at Ω, is created at the axes origin, and the time-averaged potential resembles a 3-D harmonic potential, serving as a trapping potential.

The potential generated by this trap is given in Eq.1, where r_0 and z_0 are the trap dimensions, z_0 is the separation of the end-cap electrodes and r_0 is the radius of the ring electrode. Ω is the RF frequency, U_0 and V_0 are the direct current (DC) and RF potentials applied between the end-cap electrodes and the ring [17] [18]:

$$\Phi = \frac{U_0 + V_0 cos\Omega t}{2d^2}(2z^2 - x^2 - y^2), \quad d^2 = \sqrt{\frac{1}{2}r_0^2 + z_0^2} \tag{1}$$

This can be used to derive the equations of motion of a trapped particle with a mass M, and a charge Q along each axis:

$$\frac{d^2x}{dt^2} - \frac{Q}{Md^2}(U_0 + V_0 cos\Omega t)x = 0$$

$$\frac{d^2y}{dt^2} - \frac{Q}{Md^2}(U_0 + V_0 cos\Omega t)y = 0$$

$$\frac{d^2z}{dt^2} + \frac{2Q}{Md^2}(U_0 + V_0 cos\Omega t)z = 0 \tag{2}$$

Now let's define:

$$a_x = a_y = -\frac{4QU_0}{Md^2\Omega^2}, \tag{3}$$

$$q_x = q_y = \frac{2QV_0}{d^2\Omega^2}, \tag{4}$$

$$a_z = \frac{8QU}{Md^2\Omega^2}, \tag{5}$$

$$q_z = -\frac{4QV_0}{Md^2\Omega^2}, \tag{6}$$

$$\tau = \frac{1}{2}\Omega t \tag{7}$$

The equations of motion become:

$$\frac{d^2u}{d\tau^2} + (a - 2q\cos(2\tau))u = 0, \qquad u \in \{x, y, z\} \tag{8}$$

This is precisely the Mathieu differential equation. Solutions to the Mathieu equation are either:

- **Stable**: bounded and oscillatory, or
- **Unstable**: exponentially diverging.

The boundaries between stable and unstable behavior form the **Mathieu stability diagram** in the (a, q) plane as presented in Fig. 2.

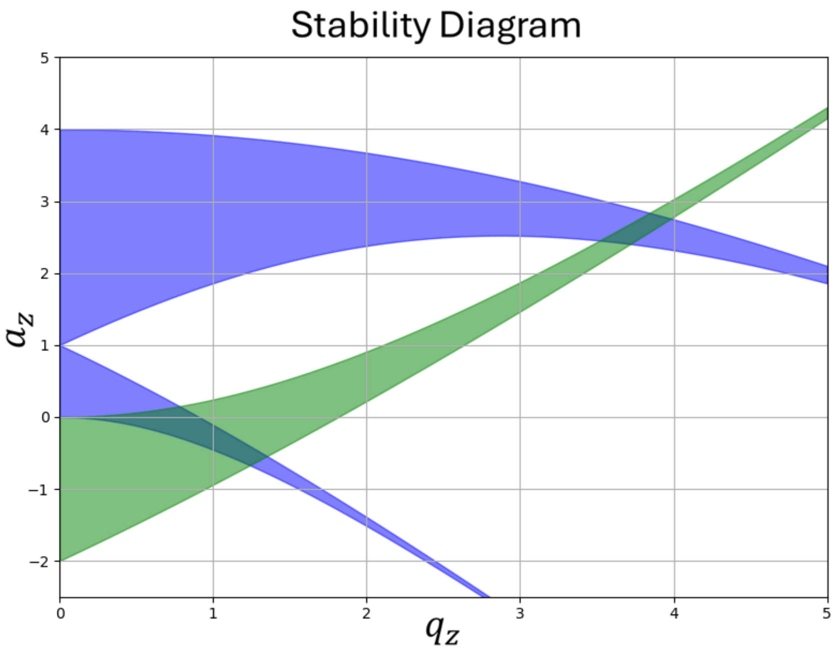

Figure 2: Mathieu stability diagram showing the stability domains of an ideal Paul trap. The shaded blue area highlights the stability region of the axial trap z axis (as defined in Fig. 1) and the green shows the same for the radial trap x and y axes. The intersection of the marked areas are the trap's stable regions. The a_z and q_z parameters are defined in Eqs. 5 and 6. The boundaries of the stability region are set by the β parameter (defined in Eq. 10). The a and q parameters (of each axis) that set a value of β as $0 < \beta < 1$ are stable. So, only a and q parameters which produce a stable solution for all axes, are considered stable in a 3-D trap.

The general solutions to the Mathieu equation are given by Floquet's theorem:

$$u(\tau) = e^{i\mu\,\tau}\,P(\tau),$$

where

- μ is the **characteristic exponent**,
- $P(\tau)$ is a periodic function of period π.

We define the **stability parameter** β by

$$\beta \;\equiv\; \mu.$$

For $\beta \in \mathbb{R}$, the solution is bounded and oscillatory. If β acquires an imaginary part, the solution grows exponentially and becomes unstable. Since $\tau = \frac{1}{2}\Omega t$, the motion can be written as:

$$u(t) \;\propto\; \underbrace{e^{\,i(\beta\,\Omega/2)\,t}}_{\text{secular motion}} \;\times\; \underbrace{P(\tfrac{\Omega t}{2})}_{\text{micromotion}}$$

So we find that in addition to the RF frequency, the solution exhibits another, slower, frequency that we shall refer to as the secular frequency. The secular (slow) oscillation frequency is:

$$\omega_{\text{sec}} \;=\; \frac{\beta\,\Omega}{2}. \tag{9}$$

The exact value of β sets the boundaries of the stability regions and is determined by the *Floquet discriminant* $\Delta(a,q)$, namely

$$\Delta(a,q) = 2\cos(\pi\beta),$$

so that

$$\beta(a,q) \;=\; \frac{1}{\pi}\,\arccos\!\big(\tfrac{1}{2}\Delta(a,q)\big). \tag{10}$$

In practice, one computes β via numerical routines for experimental a and q values.

For $q \ll 1$ and $a > 0$, a perturbative expansion gives the adiabatic approximation:

$$\beta \;\approx\; \sqrt{a + \tfrac{q^2}{2}} \quad\Longrightarrow\quad \omega_{\text{sec}} \approx \frac{\Omega}{2}\,\sqrt{a + \tfrac{q^2}{2}}\,.$$

2.1.2 End-cap Paul traps

The ideal Paul trap design (Fig. 1) prohibits optical access to the trapped particles, which is crucial for detecting the motion of the particle. Therefore, we chose a more "open" geometry without the ring, which still produces a trapping quadrupole potential while allowing optical access from the radial axes. This is the "end-cap trap" [19]. To quantify the deviation of the end-cap's potential from the ideal quadrupole, we introduce the trap efficiency parameter η, which describes the fraction of the applied voltage that contributes to the quadrupole component [20]. We also introduce a radial asymmetry parameter ϵ. Including these parameters, the electric potential takes the form:

$$\Phi = \frac{\eta_U U_0 + \eta_V V_0 cos\Omega t}{2d^2}[2z^2 - (1-\epsilon)x^2 - (1+\epsilon)y^2] \tag{11}$$

The main reason for breaking the radial symmetry is to make parametric cooling possible. In the ideal trap geometry, when the motion on both radial axes is out of phase, the cooling of one axis necessarily leads to heating the other. Also, it helps to better distinguish between the motion along the two axes and thus analyze the total particle motion more accurately. The η parameters can be experimentally obtained by measuring the secular frequency of each axis to find β, using it to find the Mathieu parameter q, and setting a to be zero by applying no DC voltage on the end-cap electrodes. A COMSOL simulation of the electric potential created by the end-cap trap used in our system is presented in Fig. 3.

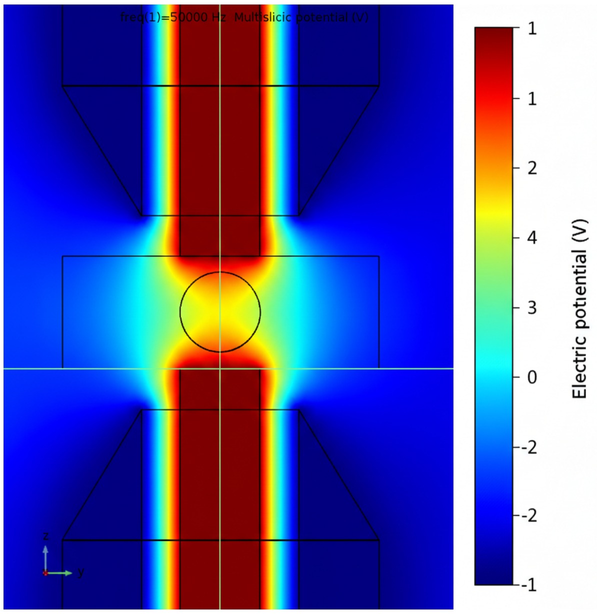

Figure 3: A COMSOL simulation, using the finite element method (FEM), of the quadrupole electric potential of an end-cap Paul trap as used in our system (following the work of [19]). The electric potentials of the two inner electrodes are set to a DC voltage of $1V$ (seen in red), while the two outer electrodes are set at $-1V$ (seen in blue). For the case of AC voltages applied to the electrodes (such as in the end-cap Paul trap), the potential at a certain position in the trapping region can be calculated using this simulation. This is done by noting the potential at this position derived from the COMSOL simulation, and simply multiplying it by the value of the applied AC voltage at a given moment. In this simulation, the inner electrodes are 1 mm in diameter and the distance between them is 1.7 mm. The same as our experimental system.

2.2 Particle loading

A Paul trap creates a conservative trapping potential, so a particle entering the trap will exit it with the same energy. Unless there is a dissipation process to reduce the kinetic energy of the particle, it will escape the trap. Currently we are using an electrospray technique [21] (see 2.2.1) under bad vacuum conditions. Here, while the particles are introduced into the chamber with high kinetic energy, collisions with background gas dampen their motion in the trap and allow stable trapping. Once a particle is trapped, the background gas can be removed by pumping until ultra high vacuum (UHV) is reached.

Alternatively, dry methods, such as laser induced acoustic desorption (LIAD) or ultra sonic launching are preferred to maintain UHV conditions. In this case, there is no damping by background gas collisions, as the particle is trapped by timing the operation of the trap with the launching of the particle [22] [23].

2.2.1 Electrospray

In the electrospraying ionization (ESI) technique, a solution of colloidal nanoparticles is introduced into the chamber through a narrow capillary held at a high electric potential (several kilovolts), causing the liquid at the tip to deform into a "Taylor cone" and emit a fine jet of charged droplets. Typically, the colloidal solution is further diluted with a volatile solvent to avoid aggregation and allow fast removal of excess solution vapor from the chamber by pumping. As these droplets travel through the electric field, solvent evaporation and Coulombic repulsion reduce their size, ultimately producing a spray of highly charged isolated nanoparticles.

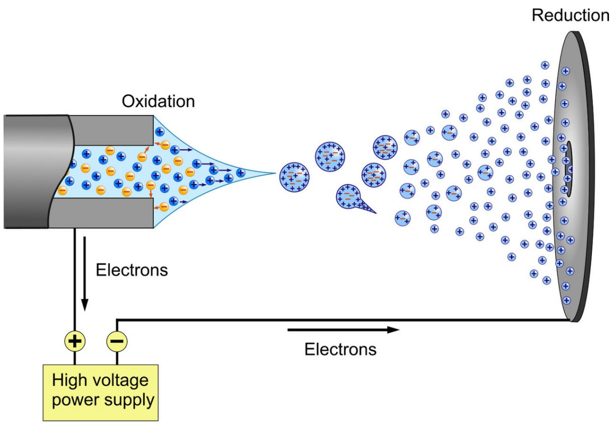

Figure 4: An illustration of an electrospray setup taken from the Wikipedia page [24]. A jet of droplets made of a carrier solvent containing the nanoparticles is emitted from the "Taylor cone", which is formed at the tip of the needle. The solvent from the droplets progressively evaporates, leaving only the charged nanoparticles in the trapping region.

2.3 Detection

2.3.1 Homodyne detection

Homodyne detection is a phase-sensitive measurement technique in which a weak signal interferes with a strong reference, often termed a "local oscillator" (LO), of the same frequency. The intensity of the resulting interference pattern is proportional to the cosine of the phase differences between the LO and the weak signal, thus allowing for phase changes to be detected by means of intensity modulations that are measured using photodiodes.

In our experiment, the LO is a laser beam of a wavelength much larger than the characteristic size of the particle. The LO is focused on the particle and induces an emission of dipole radiation. This radiation can be approximated as Rayleigh scattering, and the resulting interference pattern of the unscattered LO and the induced dipole radiation is [25]:

$$\frac{\delta I(x)}{I_{\mathrm{tot}}} = \frac{2\,k^3\alpha}{\pi\,r^2}\exp\!\left(-\frac{x^2}{w_0^2}\right)\sin\!\left(k\,x\,\sin\theta\,\cos\phi\right)\exp\!\left(-\frac{k^2\,w_0^2\,\theta^2}{4}\right) \tag{12}$$

Where:

$\delta I(x)$ Change in the detected intensity at lateral position x in the back focal plane.

I_{tot} Total power of the incident Gaussian beam.

$k = \frac{2\pi n_s}{\lambda_0}$ Wavenumber in the surrounding medium (with refractive index n_s and vacuum wavelength λ_0).

α Polarizability of the Rayleigh scatterer (particle), given by $\alpha = 4\pi\varepsilon_s a^3\,\dfrac{n_r^2-1}{n_r^2+2}$.

r Distance from the scatterer to the observation point (far–field).

x Lateral displacement of the particle from the optical axis in the focal plane.

w_0 $1/e$ intensity radius (waist) of the focused Gaussian beam.

θ Polar (scattering) angle relative to the optical axis.

ϕ Azimuthal angle in the back focal plane (with $\phi = 0$ along the x–axis).

A simulation of the intensity shifts on a back focal plane caused by the interference pattern of a LO and a dipole scatterer can be seen in Fig. 5(a). Observing the simulation, measuring the difference in intensity shifts between the right and left sides of the back focal plane can serve as a metric for particle position detection. A simulation of right-left intensity shift difference as a function of particle displacement can be seen in Fig. 5(b).

(a) (b)

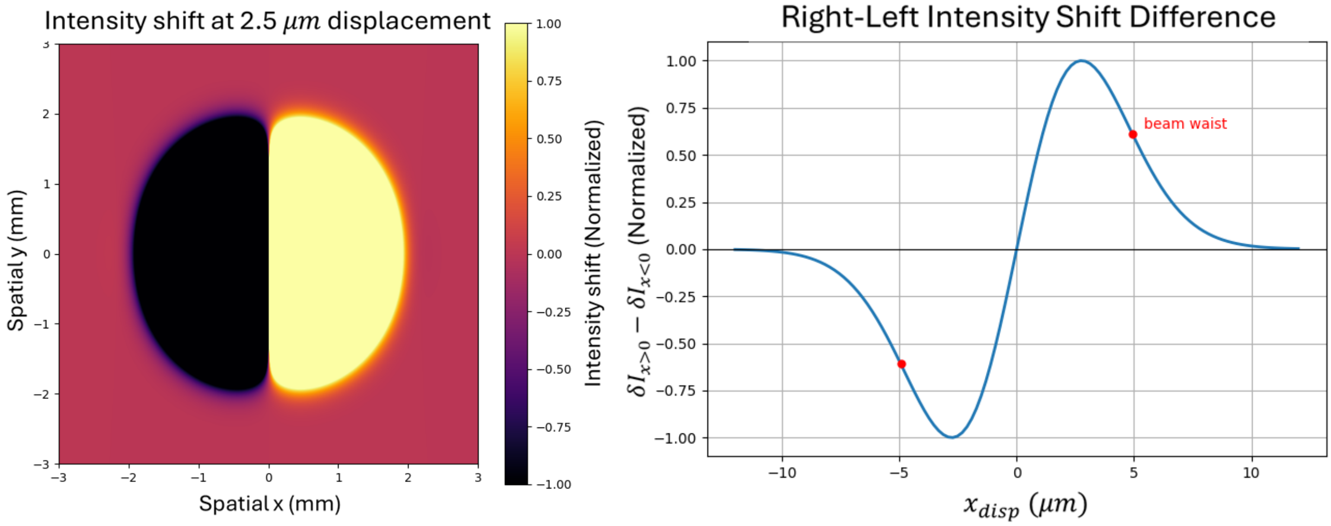

Figure 5: Simulation of the interference of a 1560 nm beam with an induced dipole scatterer. The dipole scatterer is oscillating along the radial x axis while the beam propagates along the axial z axis. (a) The intensity shifts on an x-y back focal plane 1 cm away from the beam focus caused by the displacement of the particle in the trap. Here, the particle is displaced 2.50 μm from the trap center (with a beam waist of $w_0 = 5\,\mu$m) along the x-axis. The center of oscillation is at x=y=0 and at the beam focus along the z-axis. (b) The normalized difference between the intensity shifts on the right side of the plane ($\delta I_{x>0}$) to the left side ($\delta I_{x<0}$) as a function of the displacement of the dipole scatterer along the x axis. The red dot marks the beam waist and as expected, once the particle's displacement exceeds it, the signal exponentially diminishes. There is a small oscillation regime (roughly $\pm\frac{w_0}{4}$), where this difference is linear to the scatterer displacement. Therefore, using a D-shaped mirror and a balanced photodetector (BPD) as described in 3.4, we could measure this difference in real-time, and after calibration, receive an accurate description of the particle's motion along each axis.

2.3.2 Heterodyne detection

In heterodyne detection technique, a weak optical signal is combined with a strong LO that is shifted in frequency by $\Delta\omega$. The signal and LO fields are given by:

$$E_{\text{sig}}(t) = A_{\text{sig}} e^{i\omega_{\text{sig}} t} \quad \text{and} \quad E_{\text{LO}}(t) = A_{\text{LO}} e^{i\omega_{\text{LO}} t}$$

When the two beams are superposed on a photodiode, the output contains a beat term oscillating at the difference frequency (DF):

$$\Omega_{\text{IF}} = |\omega_{\text{sig}} - \omega_{\text{LO}}|.$$

By filtering out the DC and sum-frequency components, one isolates this beatnote, whose amplitude is proportional to $2A_{\text{sig}}A_{\text{LO}}$, thus effectively amplifying the weak signal via the heterodyne cross term.

Once the DF beatnote is isolated, it can be digitized and demodulated in software or electronics to recover both in-phase (I) and quadrature (Q) components of the original field. These quadratures encode the full amplitude and phase of $E_{\mathrm{sig}}(t)$, allowing a precise measurement of signal dynamics at high sensitivity and benefiting from the rejection of low-frequency technical noise. Furthermore, compared to homodyne detection (where $\omega_{\mathrm{LO}} = \omega_{\mathrm{sig}}$), heterodyne's deliberate frequency offset avoids low frequency noise and improves the signal-to-noise ratio (SNR) of the measurement.

2.3.3 Thermometry

In the state of the art cooling in a Paul trap, the translation motion of a silica bead reached a temperature of few milikelvins [26]. The trapped particle is modeled as a harmonic oscillator, damped by collision with background gas:

$$m\ddot{x} + m\gamma\dot{x} + m\Omega_0^2 x = F_{th} \tag{13}$$

Where:

x Displacement of the particle from equilibrium on a single axis.

m Mass of the particle.

γ Viscosity coefficient.

Ω_0 Secular frequency of the trap.

F_{th} Fluctuation force due to coupling with thermal bath.

Without active cooling and at elevated pressures (over 10^{-3} mbar), the particle is in thermal equilibrium with the background gas. The thermal force F_{th} fulfills the fluctuation-dissipation theorem [27]:

$$\langle F_{th}(t)F_{th}(t+\tau)\rangle = 2m\gamma k_B T\delta(\tau) \tag{14}$$

Where T is the temperature of the particle , k_B is the Boltzmann constant and δ is the Dirac function. The system reaches equilibrium when the fluctuation force is equal to the drag force (the second term in Eq. 13). Using this and Eq. 13 we get the single-sided power spectral density (PSD) for a harmonic oscillator:

$$\hat{S}_{xx}(\Omega) = \frac{2\,k_B T\,\gamma/(\pi m)}{(\Omega_0^2 - \Omega^2)^2 + (\gamma\,\Omega)^2} \tag{15}$$

We can use the Wiener-Khinchin theorem to relate the variance of displacement to the PSD:

$$\langle x^2\rangle = \int_0^\infty \hat{S}_{xx}(\Omega)d\Omega \tag{16}$$

Which gives us the result:

$$m\Omega_0^2\langle x^2\rangle = k_B T \tag{17}$$

The detection optical signal (given in voltage V) is linearly related to the displacement for small oscillations (as seen in Fig. 5(b)), with the resulting relation $V = c_{cal}x$ for some calibration constant, giving us:

$$m\Omega_0^2 \frac{\langle V^2 \rangle}{c_{cal}^2} = k_B T \tag{18}$$

Measuring the variance at a known temperature allows us to extract m/c_{cal}^2. If the mass is known then we also have the calibration factor. In practice, we can measure the variance in two ways: in the time-domain by analysis of the position measurements, or in the frequency domain by integrating over the peak around Ω_0 (see Eq. 16). Both ways give us a measured value proportional to the particle temperature. Thus, calibration at thermal equilibrium in room temperature allows temperature determination under active cooling, even when the background gas is already pumped out and the particle is under high vacuum conditions.

In some cases, dry loading is performed under UHV conditions [22, 23]. In these cases, calibration under thermal equilibrium is not possible and direct determination of the particle mass and c_{cal} is necessary. Sometimes the mass is known if the particle specifications are provided. c_{cal} can be measured directly by tracking the particle position with a camera [28].

When reaching the ground state, Stokes and anti-Stokes measurements are needed to calculate the phonon occupation number. This method of measurement has demonstrated ground state cooling for optically levitated nanoparticles [13].

2.4 Active cooling of a trapped particle

In this work, we employed two active cooling methods: Parametric feedback and electric velocity damping. The optimal feedback gain and minimal temperature can be analytically calculated for both methods [29].

2.4.1 Electric velocity damping

The secular motion of the particle on a single axis in the trap can be written as $x(t) = Acos(\omega t)$. In electric feedback cooling, the particle is slowed down by introducing an external electric field, which counters the particle's motion and can be viewed as a damping viscous force. Therefore, the particle would experience an electric force which is also harmonic with a change in amplitude and phase $F_{fb}(t) = \gamma_{fb}cos(\omega t + \phi)$ [26]. Both the feedback gain γ_{fb} and phase ϕ are experimentally optimized. Using trigonometric identities, the feedback force can be written as:

$$F_{fb} = \gamma_{fb}cos(\omega t)cos(\phi) - \gamma_{fb}sin(\omega t)sin(\phi) = \frac{\gamma_{fb}}{A}cos(\phi)x(t) + \frac{\gamma_{fb}}{A\omega}sin(\phi)v(t) \tag{19}$$

The feedback force is decomposed into two quadratures of motion, one of position and another of velocity. For $\phi = -\frac{\pi}{2}$ it is a purely cooling force and for $\phi = -\frac{3\pi}{2}$ it is pure heating. At any other phase we get a force with an unwanted position-dependent term.

To find the optimal gain and minimal temperature, we revise the model of the damped driven harmonic oscillator seen in Eq. 13 to include measurement noise and velocity-dependent feedback:

$$\ddot{x} + \gamma_0 \dot{x} + \gamma_{fb}(\dot{x} + \delta \dot{x}) + \Omega_0^2 x = \frac{F_{th}}{m} \tag{20}$$

Where γ_{fb} is the damping due to feedback and $\delta \dot{x}$ is stochastic noise in the feedback signal caused by noise in the measurements and electronics. Eq. 20 is valid in a vacuum range down to about 10^{-7} mbar, where thermal forces due to collision with background gases are dominant. At lower pressures, other forces, such a coupling to electric noise from the environment, cannot be neglected and the equation of motion should be modified. Using Fourier analysis and Wiener-Khinchin theorem gives us [30]:

$$T = T_0 \frac{\gamma_0}{\gamma_0 + \gamma_{fb}} + \frac{1}{2} \frac{m\Omega_0^2}{k_B} \frac{\gamma_{fb}^2}{\gamma_0 + \gamma_{fb}} S_{nn} \tag{21}$$

Where S_{nn} is the detection noise spectral density, assumed to be uncorrelated white noise. In the limit $\gamma_{fb} >> \gamma_0$ the optimum feedback gain is given by:

$$\gamma_{fb} = \sqrt{\frac{2\gamma_0 k_B T_0}{S_{nn} m \Omega_0^2}} \tag{22}$$

Which yields the minimal temperature:

$$T_{min} = \sqrt{\frac{2 S_{nn} m \Omega_0^2 \gamma_0 T_0}{k_B}} \tag{23}$$

2.4.2 Parametric feedback

Parametric feedback cooling is a technique used to reduce the energy of a system by modulating a parameter of the trapping system in time. For example, we can consider a harmonic oscillator as the system we wish to cool, so the modulated parameter would be the trap stiffness. If this parameter is periodically modulated at twice the trap frequency (in our system it would be the secular frequency), the motion of the oscillator either grows to instability or is suppressed and cooled down, depending on the phase of the modulation. We have performed parametric cooling by modulating the driving voltage (see Fig. 14 for results). In general, the limit of cooling by parametric feedback is comparable to that of velocity damping [29].

2.5 Kalman Filter

2.5.1 Introduction to Kalman filtering

The Kalman Filter [31] is an iterative algorithm used to filter out noise from measurements of the state of a system in real-time. In each time-step, the algorithm receives the current state measurement values, the previous state estimation values, and the covariances of both, based on the assumption that all values behave as Gaussian random variables. In addition, the algorithm must know the physical behavior and properties of the system, so that if given the state estimation from the previous step it could provide a current state prediction based on the evolution of the system in time. The algorithm calculates the current state estimation by a weighted mean of the current state measurement and the current state prediction (derived by propagating the previous state estimation through time using classical motion equations). The weights of the measurement and of the prediction depend on the covariances of each. The larger the covariance, the smaller the weight. This weighted mean is considered to be closer to the true state than the actual data measurement.

The algorithm itself consists of two steps, prediction and measurement. In the prediction step, the previous state estimation and its covariance are used to make a prediction of the current state:

$$\boldsymbol{x_{t,t-1}} = \Phi \boldsymbol{x_{t-1,t-1}} \tag{24}$$

$$P_{t,t-1} = \Phi P_{t-1,t-1} \Phi^t + Q \tag{25}$$

Where $\boldsymbol{x_{t,t-1}}$ is the current state prediction, $\boldsymbol{x_{t-1,t-1}}$ is the previous state estimation, Φ is the state propagation matrix, $P_{t,t-1}$ is the prediction covariance, $P_{t-1,t-1}$ is the previous state estimation covariance and Q is the process noise.

In the following measurement step, the algorithm receives the current state measurement and then calculates the current state estimation as a weighted mean of the measurement and the prediction:

$$K_t = P_{t,t-1} H^t (H P_{t,t-1} H^t + R)^{-1} \tag{26}$$

$$\boldsymbol{x_{t,t}} = \boldsymbol{x_{t,t-1}} + K_t (y_t - H \boldsymbol{x_{t,t-1}}) \tag{27}$$

$$P_{t,t} = (I - K_t H) P_{t,t-1} (I - K_t H^t) + K_t R K_t \tag{28}$$

Where K_t is the Kalman gain at time step t (the weight of the weighted mean), H is the measurement matrix that relates the state vector to the measured signal, R is the measurement noise, $\boldsymbol{x_{t,t}}$ is the current state estimation and $P_{t,t}$ is its covariance.

The best practice is to apply this algorithm to the measurements of the position of the trapped nanoparticle in order to filter out noise and achieve a more reliable description of its motion.

2.5.2 Implementation

In our experiment, precise measurements of the state of the system are crucial both for an accurate description of the trapped particle and to achieve optimal cooling. To this end, we attempted to implement a Kalman Filter algorithm in our system.

First, we model the CoM motion of the particle on each axis as an independent damped oscillator. In reality we know that a particle in a Paul trap exhibits motions at two separate frequencies on each axis: the AC drive frequency and a secular frequency. The motion at the drive frequency, noted as the micromotion, will be overlooked by the Kalman algorithm for two reasons. Firstly, the simplicity of the algorithm will save us valuable computing time. Secondly, the Kalman algorithm is set to cool the particle by means of electric feedback, which will be ineffective for it. The secular motion on each axis is then given by:

$$m\ddot{x}(t) = F_0 + F_\gamma(t) \tag{29}$$

Where $x(t)$ is the position on x-axis at time t, and m is the mass of the particle. The term F_0 accounts for the harmonic trap force at the secular frequency:

$$F_0 = -kx(t) = -m\Omega_x^2 x(t) \tag{30}$$

The term F_γ accounts for the drag force:

$$F_\gamma = -\gamma(t)\dot{x}(t) = -(\gamma_0 + \gamma_{fb}(t))\dot{x}(t) \tag{31}$$

Where γ_0 is the damping due to collisions with gas molecules and γ_{fb} is the damping from the applied feedback force.

We then set the state vector $\boldsymbol{x(t)} = (x(t), \dot{x}(t))^t$ to portray Eq.29 in the state space form:

$$\dot{\boldsymbol{x}} = \begin{pmatrix} 0 & 1 \\ -\Omega_x^2 & -\frac{\gamma}{m} \end{pmatrix} \boldsymbol{x} = A\boldsymbol{x} \tag{32}$$

Where A is denoted as the time derivation matrix. Solving the continuous temporal equation gives us the state propagation matrix:

$$x(t) = e^{At}x(0) \tag{33}$$

However, the Kalman filter uses discrete time steps with a certain sampling period T_s. So to propagate the system from time step t to $t + T_s$:

$$x_{t+T_s} = \Phi x_t \tag{34}$$

Where:

$$\Phi = e^{AT_s} = I + AT_s + \frac{1}{2}(AT_s)^2 + ... \tag{35}$$

To find Φ we must diagonalize A. We find the eigenvalues to be: $\lambda_{1,2} = -\frac{\gamma}{2m} \pm \sqrt{(\frac{\gamma}{2m})^2 - \Omega_x^2}$ With the corresponding eigenvectors: $v_{\lambda_1} = (1, -\frac{\gamma}{2m} + \sqrt{(\frac{\gamma}{2m})^2 - \Omega_x^2})^t$ and $v_{\lambda_2} = (1, -\frac{\gamma}{2m} - \sqrt{(\frac{\gamma}{2m})^2 - \Omega_x^2})^t$

Assuming we are in the under-damped region, that is $(\frac{\gamma}{2m})^2 < \Omega_x$, and set P as the transition matrix to the diagonalizing base, we get:

$$\Phi = e^{AT_s} = P \begin{pmatrix} e^{\lambda_1 T_s} & 0 \\ 0 & e^{\lambda_2 T_s} \end{pmatrix} P^{-1} = e^{-\frac{\gamma}{2m}T_s} \begin{pmatrix} \frac{\gamma}{2m}sin(\omega T_s) + cos(\omega T_s) & \frac{1}{\omega}sin(\omega T_s) \\ -\frac{\Omega_x^2}{\omega}sin(\omega T_s) & \frac{\gamma}{2m}sin(\omega T_s) + cos(\omega T_s) \end{pmatrix} \tag{36}$$

where $\omega = \sqrt{\Omega_x^2 - (\frac{\gamma}{2m})^2}$. Once we obtain Φ we can proceed to implement the algorithm as described in the previous chapter.

3 Experimental Apparatus

This chapter describes the experimental apparatus, which was built by Omer Feldman, a fellow M.Sc student in our group, and myself, under the supervision of Dr. David Groswasser. Its main parts consist of a vacuum chamber, which contains the Paul trap on a 3-D piezo nanometric stage; an ESI loading system; an optical system for detection, comprising BPDs that are sensitive to changes caused by the movement of the trapped particle from the trap's center along each axis; and a cooling system based on a Red Pitaya (RP) FPGA card that collects the signal from the BPD, analyzes it in real-time, and generates a ”correction signal”, which eventually is applied to electrodes surrounding the trapping region to counteract the motion of the particle. A detailed description of the various parts of the apparatus appears in the following subsections.

3.1 Red Pitaya

In most levitodynamic experiments, active feedback cooling is often performed with the aid of a RP board, which is particularly useful for its high speed FPGA technology. It comes with a package of supporting software such as a function generator (FG), spectrum analyzer, and IQ module. The latter is the most frequently used software in our experiment, as it can be used as a bandpass filter to produce a clean position-dependent signal and derive a cooling feedback from it.

In Paul trap experiments, the precise knowledge of the instantaneous position and motion of the charged particle is crucial for active cooling. The trap RF and secular frequencies are in the 5-50 kHz range, so meaningful perturbations can occur on a microsecond timescale. This means that the feedback system must acquire, process, and respond to the analogue detection signals at a sub-microsecond latency. To meet these stringent requirements, we employ the FPGA-based RP platform that provides two 14-bit ADC channels and two 14-bit DAC channels operating at a sampling rate of up to 125 MS/s (corresponds to 8 ns sampling time) and bandwidth of DC-60MHz.

The performance of the IQ module of the RP is shown in Figs. 6 and 7.

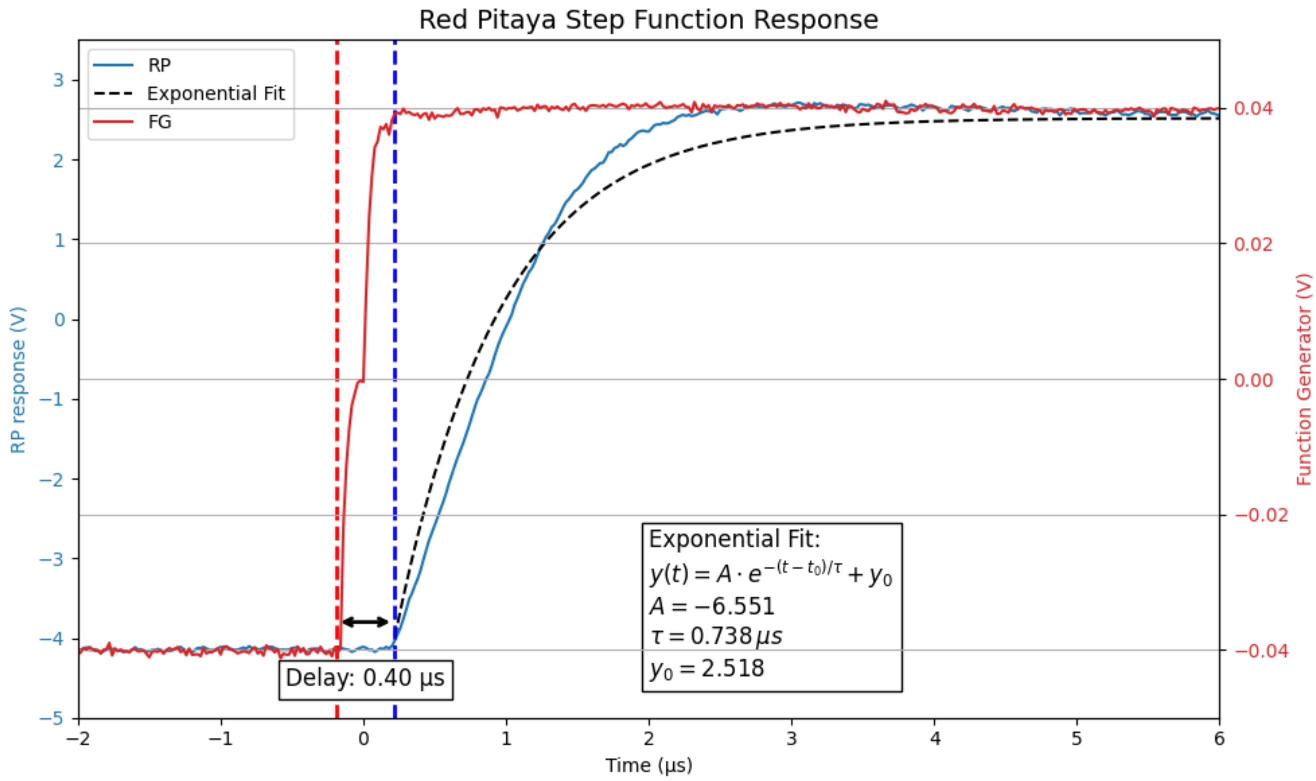

Figure 6: Analysis of the RP signal in response to a step function voltage input from an external FG at 1M ohm input impedance. The red curve shows the input step function. The blue curve shows the RP output, which was set to match the input. The vertical red dotted line represents the trigger instance of the FG step function. The blue one represents the response instance of the RP in following real-time signals. The difference between those times exhibits the delay in the RP response. This graph shows the limits of the RP to follow real-time signals, consisting of a $0.4\,\mu$s systematic delay and a $0.7\,\mu$s rise time. This is just a qualitative plot and in the future error-bars will be included to estimate the limit of cooling by the RP.

(a)

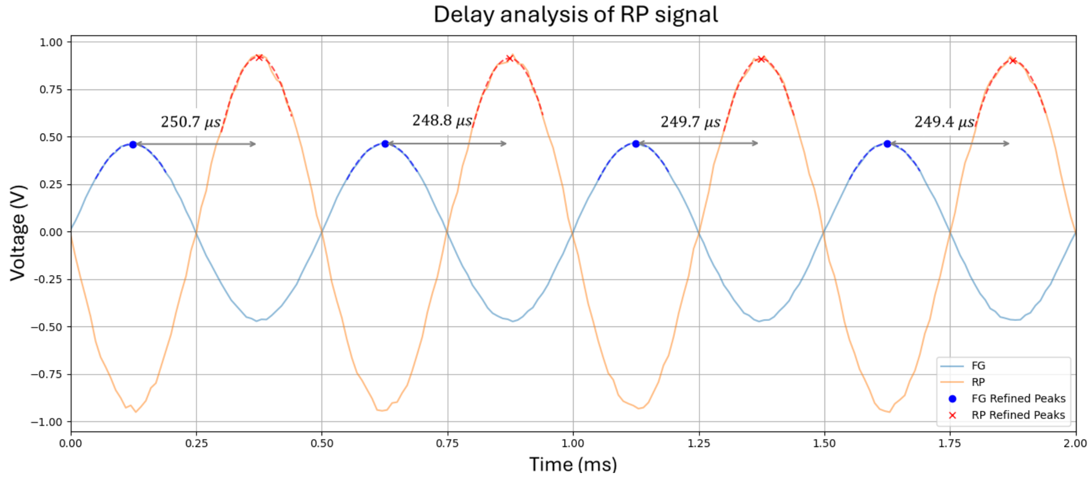

(b)

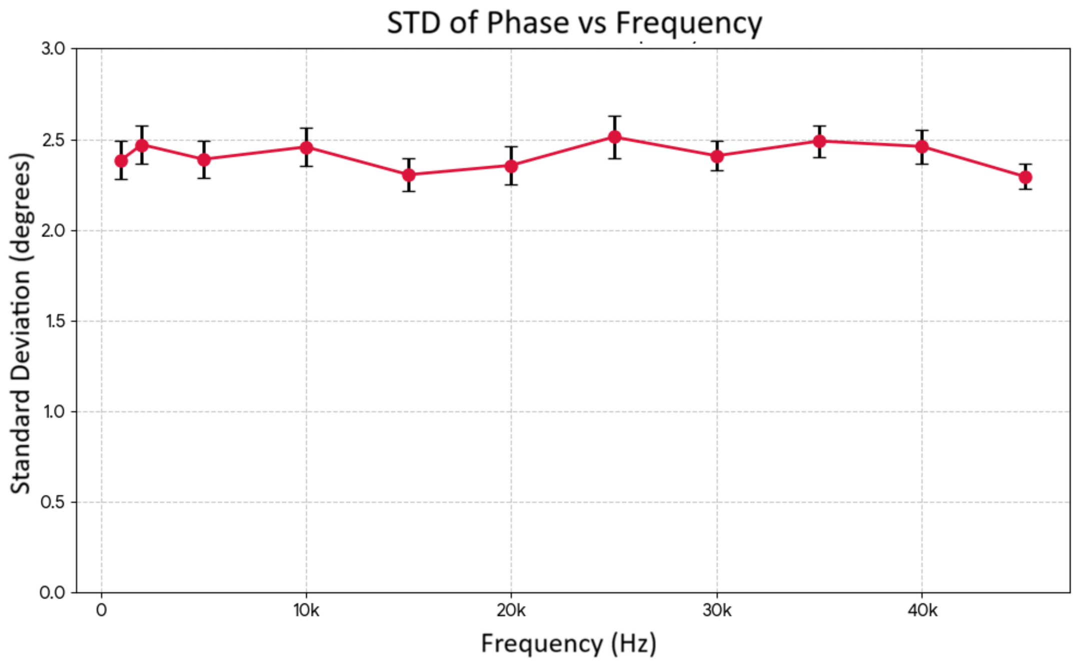

Figure 7: (a) Demonstration of the RP's IQ module ability to replicate a sine wave in real-time. The FG signal (seen in blue) is a sine of 2 kHz and the RP (seen in red) is set to return the waveform with a 180-degree phase shift. Therefore, the expected time delay between corresponding peaks is 250 μs. (b) The time delays between peaks are converted to phase delays, which can then be used to calculate the standard deviation (STD) of phase delays from the RP signal. The plot shows the STD of the phase delay for various FG frequencies. For each frequency, over 300 cycles were measured and used for the STD calculation. The error bars are the result of a uncertainty in the measured time difference between peaks over the square root of the number of cycles.

3.2 Vacuum system

Cooling a trapped particle needs to be realized under vacuum conditions, to avoid collisions and thermalization with the background gas. We use a CF160 spherical octagon from Kimball Physics. The Paul trap is assembled on a 3-D piezo stage (TSDS-255S by OptoSigma) that is mounted on the bottom flange of the chamber, so that the trap can be precisely translated to the middle of it. Pressures below 10^{-6} mbar are achieved by a multi-stage pumping system, which includes a turbomolecular pump and a getter ion pump. Both are connected to the chamber by a CF40 valve and a needle valve to allow accurate control of the chamber's background gas pressure.

The chamber has eight CF40 ports on its sides, one for pumping, one for particle loading, one for all the electrical connections, and the remaining five are fixed with view-ports to allow optical access. A CF160 flange is connected to the bottom of the chamber and is used as a mounting basis for the piezo stage. The top of the chamber is closed by a CF1060 port, allowing visualization.

3.2.1 Loading system

For reasons discussed in 2.2 we decided to use the ESI method for loading particles to the trap. Our ESI system was designed and built in-house. A schematic model is presented in Fig. 8. The design is based on a peek block with an electrical contact (normally carries 1.9-2.4 kV) to a removable needle. Loading nanoparticles into the Paul trap occurs at atmospheric pressure. We use a solution of nanoparticles that is diluted in ethanol and injected with a syringe connected to the needle by a short flexible tube. A CMOS camera is placed above the top view-port to observe light scattering from trapped particles. Once a trapped particle is detected, the needle with excess solution is extracted, and the vacuum port can be quickly closed with a KF40 blank. The turbo pump can lower the pressure to the 10^{-6} mbar range in less than 1 hour. The vacuum then slowly improves over time.

If more than one trapped particle is observed, at this stage it is possible to remove excess particles from the trap. The ejection of particles is performed by gradually increasing the drive RF frequency, lowering the trap depth until only a single particle with the highest charge-to-mass ratio remains.

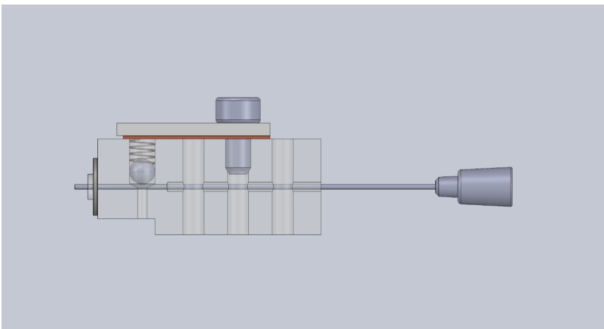

Figure 8: A SolidWorks model of the PEEK block ESI system. A stainless steel screw on the top of the block is connected to a high voltage (HV) source and in electrical contact with the needle via a metal ball pressed against it by a spring. A grounded circular electrode is placed at the end of the block, near the tip of the needle, creating the high potential difference that is necessary for ESI.

3.3 Trapping system

We operate an end-cap Paul trap geometry (see Fig. 9(a)). Each end-cap consists of an inner electrode and an outer electrode, which are insulated from each other by a PEEK sleeve. In addition, an imperfection is artificially introduced to the outer electrode to break the radial symmetry. The electrical scheme is depicted in Fig. 9(b). The AC trapping voltage is produced in the following manner: an Agilent 33220A function generator creates sinusoidal voltage, which is passed through a phase inverter, creating a second sinusoidal signal that is phase shifted from the original one by π. The two signals are then enhanced by a pair of HV amplifiers (A-304, A.A.Lab-Systems) and applied to a set of trapping electrodes, with one signal to both of the inner electrodes, and one signal to the outer ones.

The trap and its holder are placed on top of a 3-D nano-positioning piezo stage (TSDS-255S by OptoSigma) for perfect alignment of the trap center with the focus of the optical system. Two additional compensation electrodes are placed below the trap center.

(a) (b)

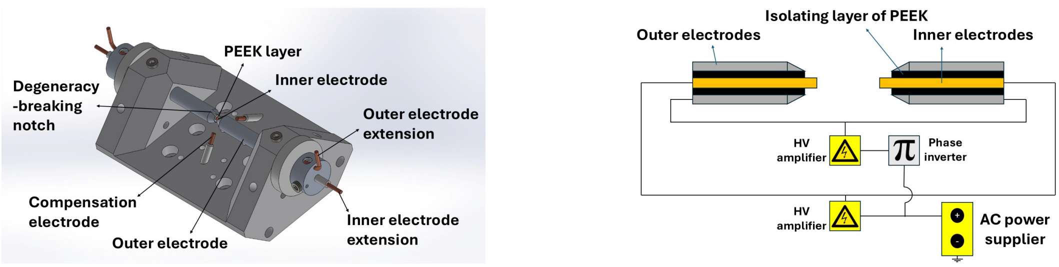

Figure 9: (a) A 3-D SolidWorks model of the end-cap trap and its holder. The compensation electrodes are used to cancel stray electric fields in the trap area that may cause a displacement of the particle from the trap center. (b) A simplified scheme of the electrical circuit of the end-cap trap. The AC voltages on the pairs of inner and outer electrodes are identical except for a π phase shift between them.

3.4 Detection system

A schematic description of the detection system appears in Fig. 10. It is based on a 1560 nm, 20 mW, RIO telecom laser and a 532 nm, 500 mW, GEM laser.

The 532 nm beam is used for camera detection of the particle and for NV spectroscopy and spin control (not a part of this thesis). The infra-red (IR) RIO laser is used for homodyne detection. The two laser beams are overlapped and focused at the trap center by an aspheric lens, NA= 0.67. The focused IR beam induces dipole radiation from the particle, with the forward dipole scattering and the un-scattered IR laser beam collimated using a second aspheric lens, NA= 0.25. The collimated beams are directed to a set of detectors where position-dependent interference between them occurs. A non-polarizing beam splitter cube (NPBS) reflects 30% of the collimated beam for x-axis motion detection using a single photodiode. The transmitted light is split for motion detection along the y and z axes. Here, we use D-shaped "edge" mirrors and BPDs (FEMTO HBPR-100M-60K-IN-FST or Thorlabs PDB250C) to generate the position sensitive signals. On both axes, the mirror's edge is orthogonal to the axis orientation. The photodetectors are balanced by aligning the beams to the edge of the D mirrors when there is no particle in the trap. The beams are split into two halves, one reflected by the mirror and one not. When each half hits one of the photodiodes, the resulting reading under such conditions is zero. A moving particle will induce an interference pattern at the mirror, which is detected by the differential signal of the photodiodes.

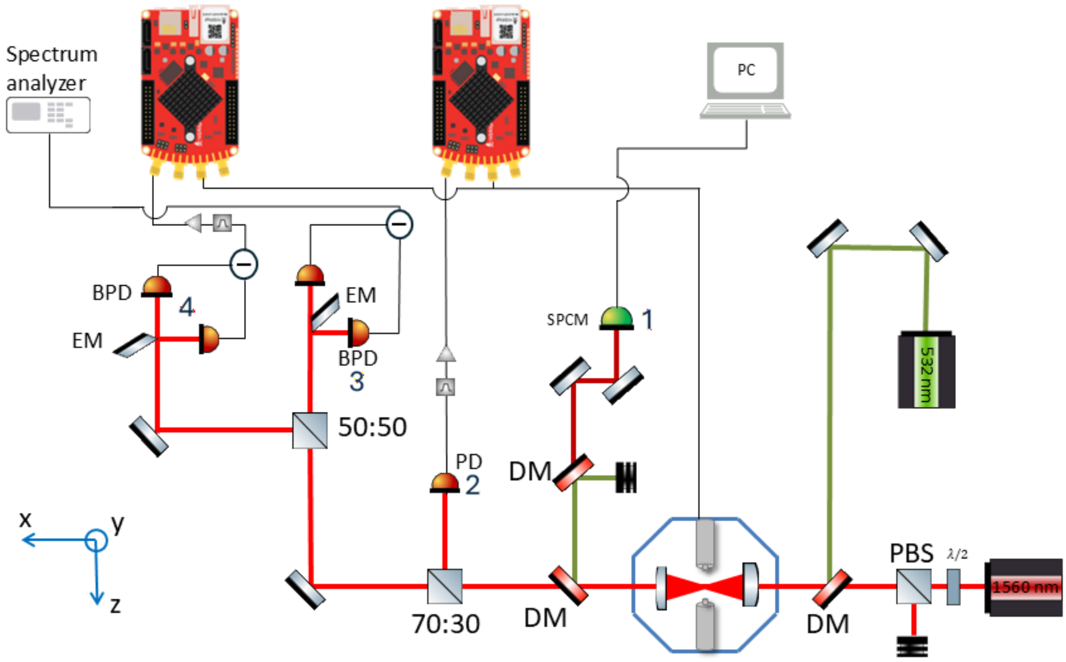

Figure 10: A schematic drawing of the experimental setup. A 1560 nm laser, which provides three-axes position detection, is intensity-controlled using a waveplate and polarizing beam splitter (PBS), then co-aligned with a 532 nm laser, which enables NV center measurements and manipulation [32, 33], before passing through the vacuum chamber to illuminate the particle. The outgoing beam is directed into a four-detector split detection array, each marked with a small dark blue number. A pair of dichroic mirrors (DM) filter out 1560 and 532 nm light, leaving only the red fluorescence of the NV center, which is detected by a single-photon counting module - SPCM (1). The photodetector - PD (2) is responsible for z axis motion detection. Balanced photodetectors - BPD (3,4) are in charge of motion detection along x and y axes. The edge mirrors (EM) deflect half of each beam to a seperate PD of the BPD as part of the detection scheme discussed in 3.4. The upgraded setup, built after I finished my work in the lab, also has a backward detection scheme, which has the advantage that the detection system is not overwhelmed by a very strong non-scattered beam.

3.5 Cooling system

An effective cooling scheme requires a high bandwidth feedback system. We use the RP board equipped with a Xilinx Zynq 7010 FPGA to perform rapid speed calculations. The IQ module of the

RP is used to generate the proper cooling feedback. It acts as a bandpass filter, meaning it can filter out a range of frequencies from the input signal and output only desired frequencies. It can also double the frequency of the output signal (for the parametric cooling scheme) and shift its phase (see Fig. 11 for demonstration of the module). This phase shift property is essential for our work since, as discussed earlier, the difference between a resonant heating force and a cooling one is entirely dependent on phase. A filtered and phase shifted velocity damping feedback signal has been used as an effective cooling force for the secular motion of a trapped particle [26, 29].

However, IQ modulation can create an unwanted offset in the produced signal. This can be very problematic, since an offset in the cooling signal can push the particle from the detection beam focus, damaging the quality of the detection signal. This can be addressed two ways: filtering the signal for low DC frequencies, or employing the RP's PID module. Another method for obtaining a signal proportional to the particle's velocity on a certain axis is the Kalman filter described in 2.5.

Parametric cooling is realized in the following manner: The RP's IQ module generates a signal at twice the frequency of the motion set to be cooled, with an appropriate phase shift. This signal is connected to the back-panel modulation port of the Agilent power supply that drives the trap (see Fig. 9(b)). The trapping AC voltage generated by the Agilent is then modulated by the IQ signal. The modulating signal from the IQ module controls the variation in amplitude of the Agilent's waveform, and the depth of the variation is controlled by the modulation depth value on the Agilent. The modulation depth is expressed as a percentage, at 0% depth the amplitude value is half of the original value regardless of the modulating waveform. At 100% depth, the amplitude value is at its original value for a $5V$ modulating signal, while at $-5V$ the amplitude vanishes.

The velocity damping signal on each axis is applied to a circular electrode placed close to the trap center (see Fig. 12), orthogonally to the axis, creating an axial electric field to counter the motion on that axis. Once the RP receives 3 signals proportional to the particle's position on each axis, it produces feedbacks proportional to the particle's velocity and applies it to the corresponding cooling electrodes. For a given particle and trapping parameters, the gain and phase of the feedback signal are optimized manually to reach the lowest temperature (See Fig. 17(a) for cooling in various pressures. According to Eq. 23, the minimal temperature scales as the square root of the pressure. However, in reality this is not valid when entering the high-vacuum regime (below 10^{-6} mbar). Then, the minimal temperature is limited by other factors, primarily the noise in the detection of the position of the particle (see Fig. 17(b)).

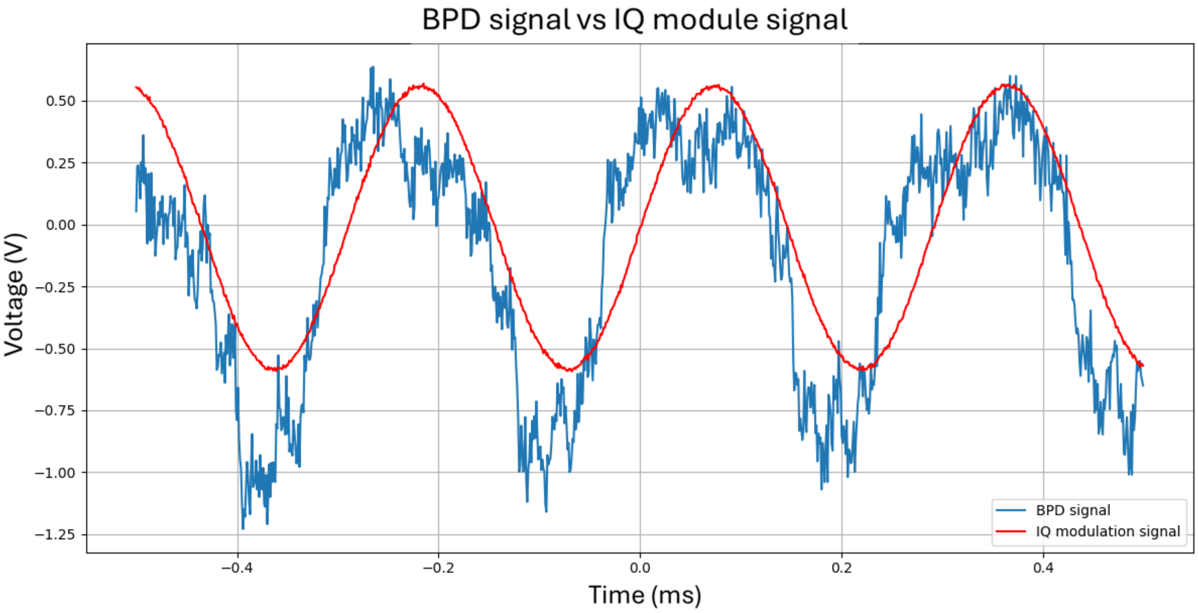

Figure 11: A demonstration of the IQ module operation in the time-domain. The noisy input blue curve is a real-time signal from the trapped particle. The input is filtered so the smoothened output red curve gives us a better description of the particle's secular motion. In this example, no phase shift is added. However, as is apparent to the eye, there is some delay between the detection signal and the IQ feedback as a result of a delay in the experiment electronics. This phenomenon also shifted the IQ phase which gets the lowest temperature, creating a need for a parameter sweep as part of the cooling procedure.

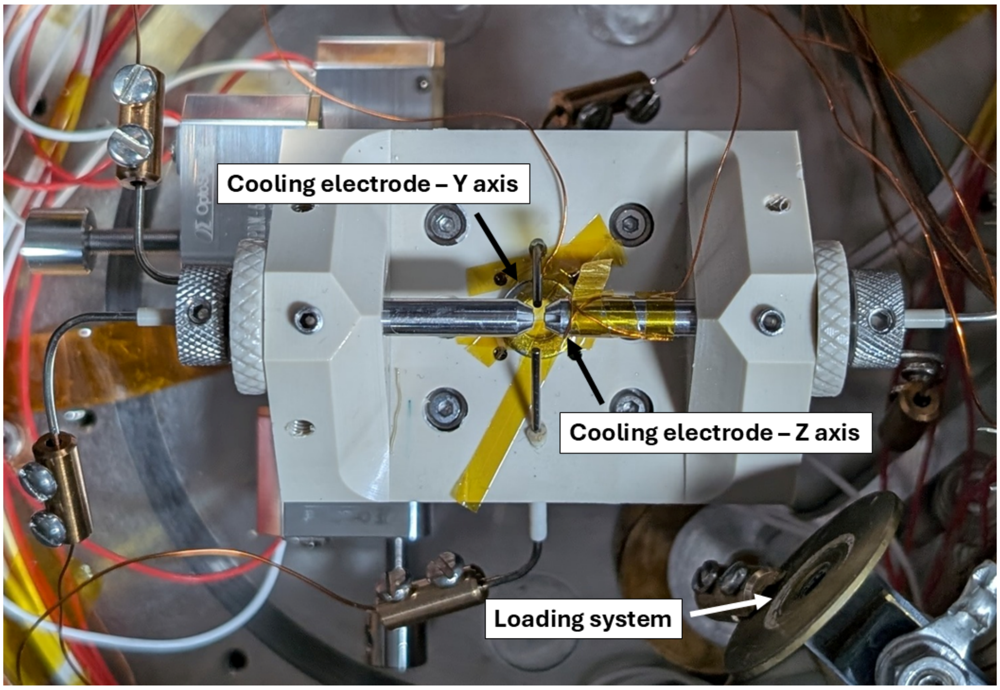

Figure 12: A top view of the end-cap Paul trap assembled on top of the 3-D piezo stage and placed inside the vacuum chamber. The y and z axes' feedback electrodes are seen, while the x axis electrode is not since it is placed on the lens mount, which had to be removed before the picture was taken. A yellow Kapton tape is used to fix the electrodes. The grounded ring electrode of the ESI loading system is observed in the bottom-right corner.

3.6 Micromotion minimization

Stray electric fields in the trap may cause the particle to be displaced from the geometrical trap center, which leads to excessive secular and micro motions. We can minimize these motions by applying bias fields from the compensation electrodes to null the stray electric fields. There are three methods for micromotion minimization [34]. The first method is to sweep across a wide range of DC voltage values on each electrode and for each axis to find the value that minimizes the micromotion peak in the PSD. The second method is to modulate the trap voltage at a certain frequency that is easily differentiated from the particle's motion frequencies. The further away the particle is from the trap center, the greater the perturbations to the particle position. To null the stray fields in the trap center, we minimize the peak in the PSD at the modulation frequency by applying DC fields. The third method is to use the RP's IQ module to produce a detection signal filtered at the drive frequency and to display it on an oscilloscope along with the trap drive voltage. The two traces are of the same frequency with some fixed phase delay between them. The phase difference between the traces is shifted by π whenever the particle's position is pushed across a null line of the trap field. So by iteratively pushing the particle across two orthogonal axes in the trap's radial plane, we can find the trap center that will minimize the micromotion.

(a)

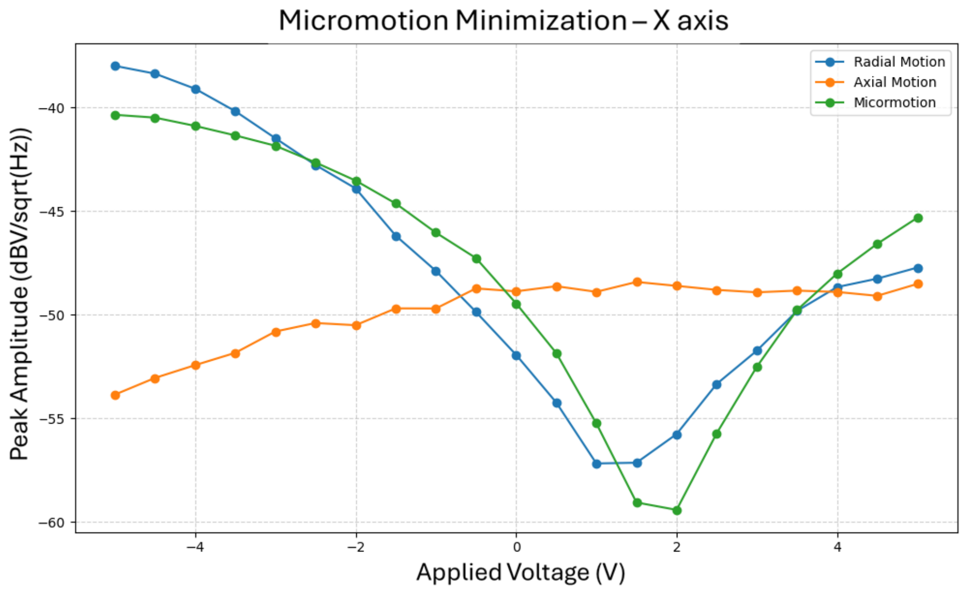

(b)

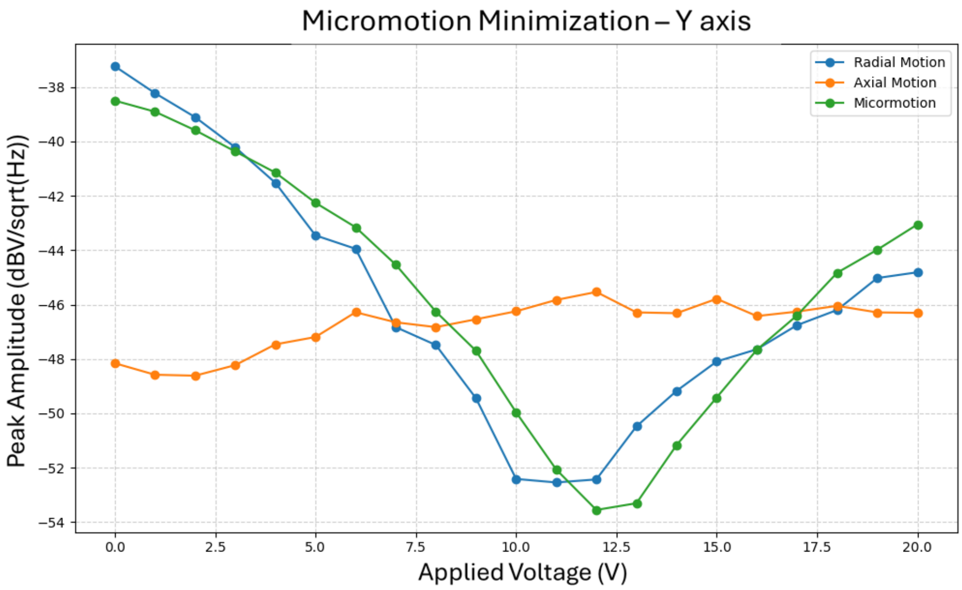

Figure 13: Micromotion minimization on x axis (a) and y axis (b) in low vacuum (1 mbar) as a probe of stray fields cancellation. We apply DC voltage on a compensation electrode on each axis and monitor the amplitude of the micro and secular motions of the particle in the PSD. (a) Compensation on the x axis. The micro and secular motions on the x axis were minimized by applying about +2 V. (b) Similarly on the y axis, minimization was achieved at about +12 V.

4 Results

4.1 Parametric cooling

Parametric cooling of CoM translation along one axis (y axis) has been demonstrated with ND particles having a diameter of 300 nm at a pressure of 5.0×10^{-5} mbar using the RP's IQ module. The output of the IQ module is used for amplitude modulation of the trap voltage. Different modulation depths were used to control the feedback influence on the particle. At greater modulation depths, the particle lost stability and was temporarily displaced from the detection beam. Fig. 14 shows the particle temperature as a function of modulation depth where the minimal temperature achieved was 15 K, alongside a PSD comparison of the particle motion for different modulation depths.

(a) (b)

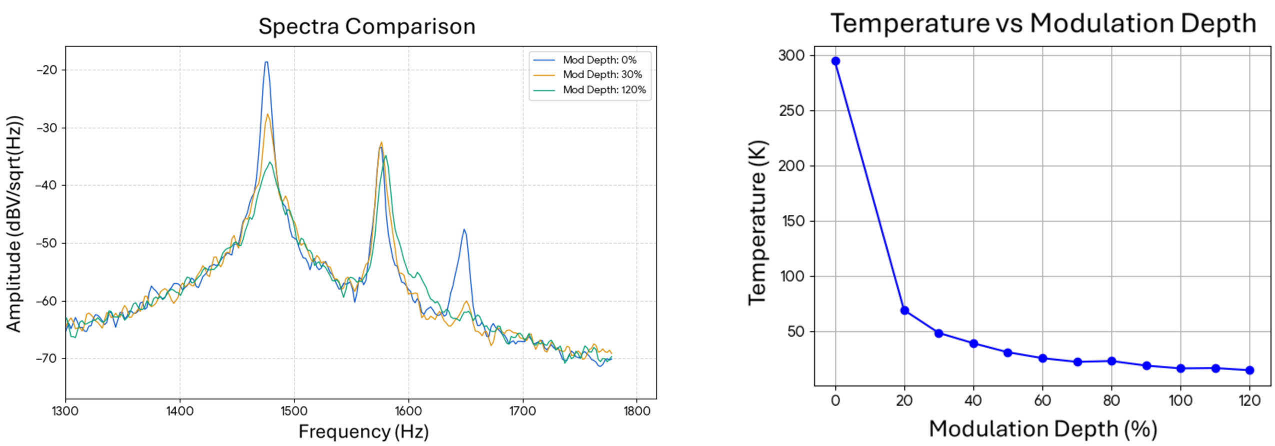

Figure 14: First parametric cooling results. The radial trap y axis and axial z axis motions are seen in the PSD. Cooling is only demonstrated on the y axis. (a) A comparison of the PSDs at different modulation depths. (b) Shows the temperature achieved as a function of the modulation depth. In the current setup, parametric cooling can reduce the temperature only by a factor of about 20, which is not satisfactory for our purposes.

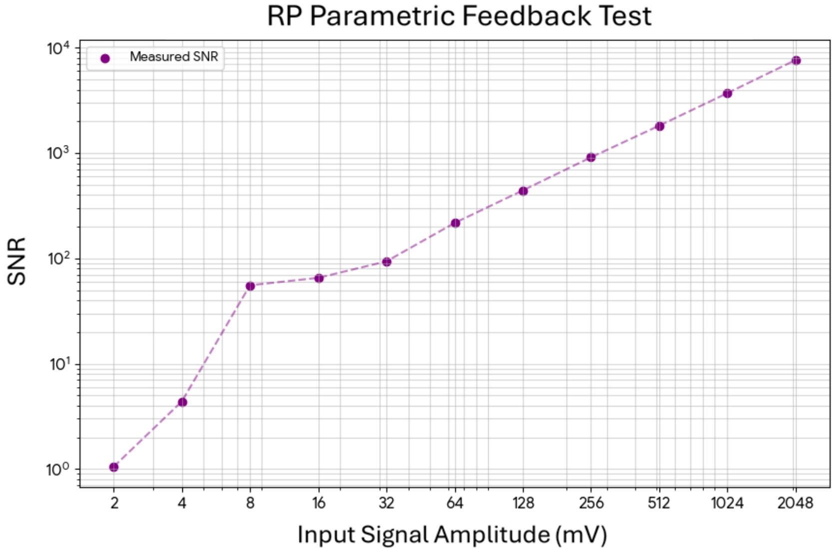

Figure 15: A plot showing the SNR of the RP's parametric feedback signal as a function of the amplitude of the input signal. As a particle is being cooled, its oscillations become smaller and harder to detect. As a result, the feedback given by the RP becomes less effective. To demonstrate this, a pure sine wave was fed to the RP's IQ module to test its reaction to detection signals of oscillations as they are being cooled, demonstrating the need for higher detection gain after a particular level of cooling. Here we can see the SNR of the parametric feedback signal reach 1 as the detection signal is reduced by 3 orders of magnitude, demonstrating the cooling limitation. This is just a qualitative plot so I did not feel the need to study the apparent kink centered around 8 mV.

4.2 Velocity damping feedback

Velocity damping feedback cooling of one axis of motion (y axis) has been demonstrated on ND particles with a diameter of 100 nm at a pressure of 8.0×10^{-5} mbar using the RP's IQ module. Fig. 16 shows the PSDs at different feedback cooling gains. A calibration trace was measured without applying a cooling feedback. The lowest temperature achieved was 570 ± 100 mK.

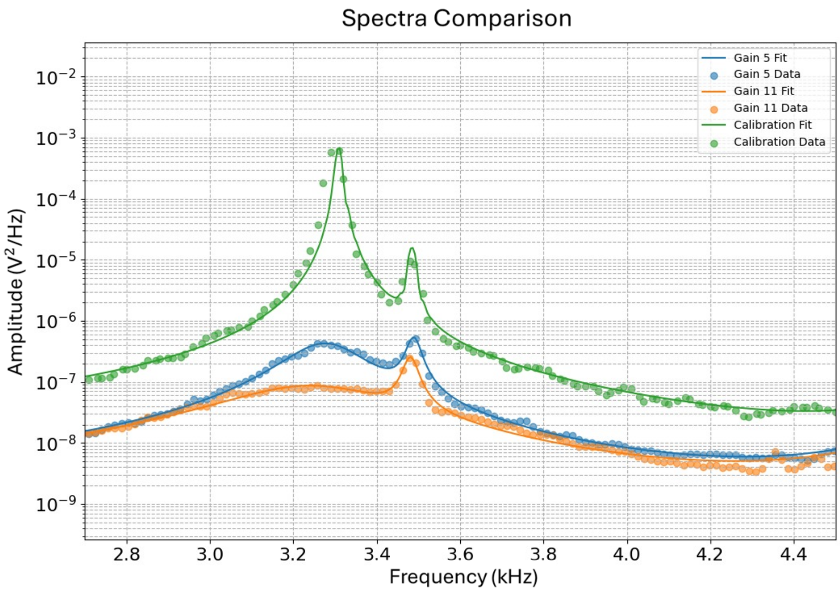

Figure 16: First sub-Kelvin cooling results. In-loop PSDs at gains of 5 and 11 (arbitrary units) measured at 8×10^{-5} mbar. A calibration trace was also measured at ambient pressure without feedback. Two modes of motion are seen in the PSDs: y and z axes. The feedback signal operates on the y axis (the lower of the two modes).

In the description above, we have assumed that without cooling, the particle is in equilibrium with the background gas at room temperature.

4.3 Cooling limitation by pressure

When observing Eq. 23, it seems that reducing the pressure should always result in lower minimal temperature. However, this is not the case, as can be seen in Fig. 17. At a low enough pressure, thermal noise becomes negligible when compared to other noise sources, such as the trap's voltage noise. Therefore, reducing pressure is very helpful for cooling, but only to a certain extent. When further reduction of the pressure is no longer effective, different measures need to be taken to minimize the temperature beyond this limit.

(a)

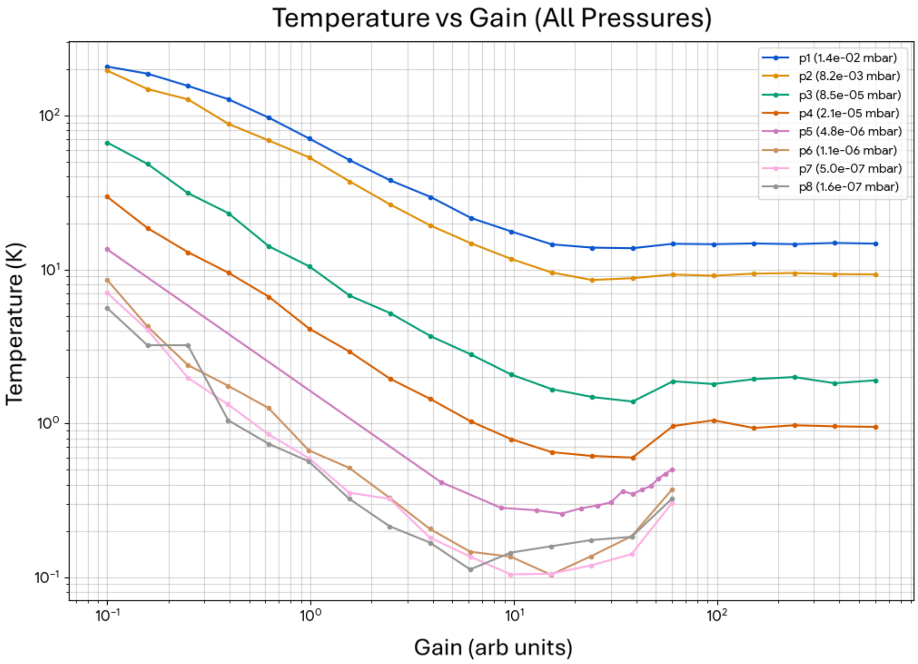

(b)

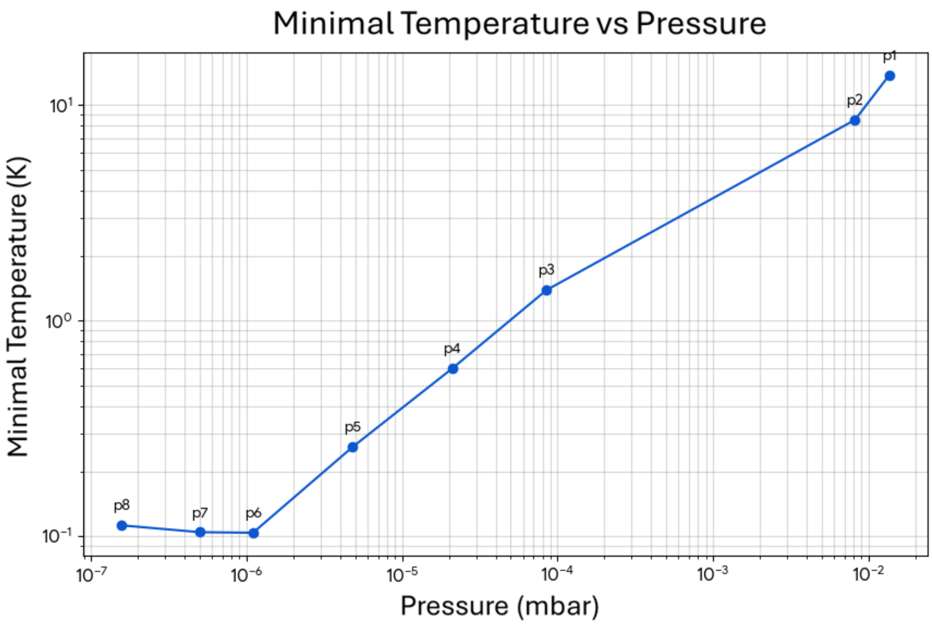

Figure 17: The minimal temperature achieved by velocity damping feedback. (a) The temperature as a function of feedback gain at different pressures. (b) The minimal temperature achieved at each pressure. Below 10^{-6} mbar the minimal temperature is not affected by further improvement of the vacuum. In this low pressure regime, thermal noise is negligible relative to other noise sources, such as voltage noise from the trap itself, which become the dominant heating source.

5 Discussion

In this thesis, CoM cooling was demonstrated using the RP's IQ module. The cooling results, presented in Figs. 14 and 16, show a complete realization of trapping, characterizing, oscillation measurement and CoM motion control of nanoparticles (both silica beads and NDs). We have cooled the CoM motion on one axis of a 100 nm diamond to sub-Kelvin temperature, comparable to state-of-the-art for diamonds of this size. At this stage, the minimal temperature is limited by detection noise. This can be improved by introducing a backward detection scheme, or higher quality diamonds, which have a smaller absorption rate and withstand higher laser power [35]. We estimate that this will enable lowering the temperature to ~1 mK, as in the case of trapped silica nano particles of similar diameter [26], and as our trap frequencies go up [36] we estimate we will be able to cool to a few μK, as was done for silica beads in high-frequency optical tweezers. Further improvements are necessary to deal with electronic noise that couples to and heats the particle. Another improvement that we will have to introduce to our system is a better evaluation of the particle position in real-time by Kalman Filtering. This method has been theoretically studied and tested by us, but currently we have not fully introduced it into the experiment due to the lack of digital signal processing power. Magrini *et al* [13] described the steps necessary to overcome this problem, and we have discussed the issue with engineers in their group. To implement their suggested code properly, we will need to find an FPGA engineer capable of rewriting the algorithm to perform Kalman filtering in asymptotic form, which reduces both accuracy and computational power. A second option is to enhance our FPGA hardware, as demonstrated in [37].

It should be noted that the physical model of the system changes at lower pressures (as demonstrated in 4.3) where thermal noise is no longer the dominant driving force. This can be potentially devastating for the Kalman algorithm, as it is highly dependent on the physics of the system to predict the state of the particle. A more reliable equation of motion must be used in the algorithm to give accurate predictions for the particle's state at lower pressure.

It should also be noted that detection sensitivity is eventually limited by the dynamic range of the RP. As the detection signal is reduced, the SNR is also reduced, as seen in Fig. 15. We suggest using automatic gain control of the signal entering the RP in combination with adaptive gain control, as described in [38].

In conclusion, cooling of ND particles in a Paul trap to sub-Kelvin temperatures puts us on par with the state-of-the-art [39]. Both active cooling methods have been implemented by the RP's IQ module. Lower temperatures can be achieved by enhancing the sensitivity of the measurements for a more accurate picture of the particle's dynamic state, and reducing the electronic noise. Finally, this thesis represents a significant step towards the final goal of matter-wave interferometry with a massive particle.

Appendices

Appendix A - Testing experiment

This appendix describes a test system that investigates the effectiveness of our cooling system and was developed before a particle was stably trapped. It is comprised of a glass slide, which is glued on a piezo crystal. A 1560 nm beam is transmitted through the glass and deflected by the vibrations caused by the piezo crystal. The deflection is detected by a BPD. A fast feedback signal is then applied to ”cool” the signal on the BPD.

This experimental apparatus consists of a RIO telecom 1560 nm laser, glass pane glued to a piezo crystal, D shaped mirror, BPD model PDB230C from ThorLabs, polarized beam splitter (PBS), linear polarizer, RP card, HV amplifier, AGILENT scope and SRS spectrum analyzer. The setup is presented in Fig. 18.

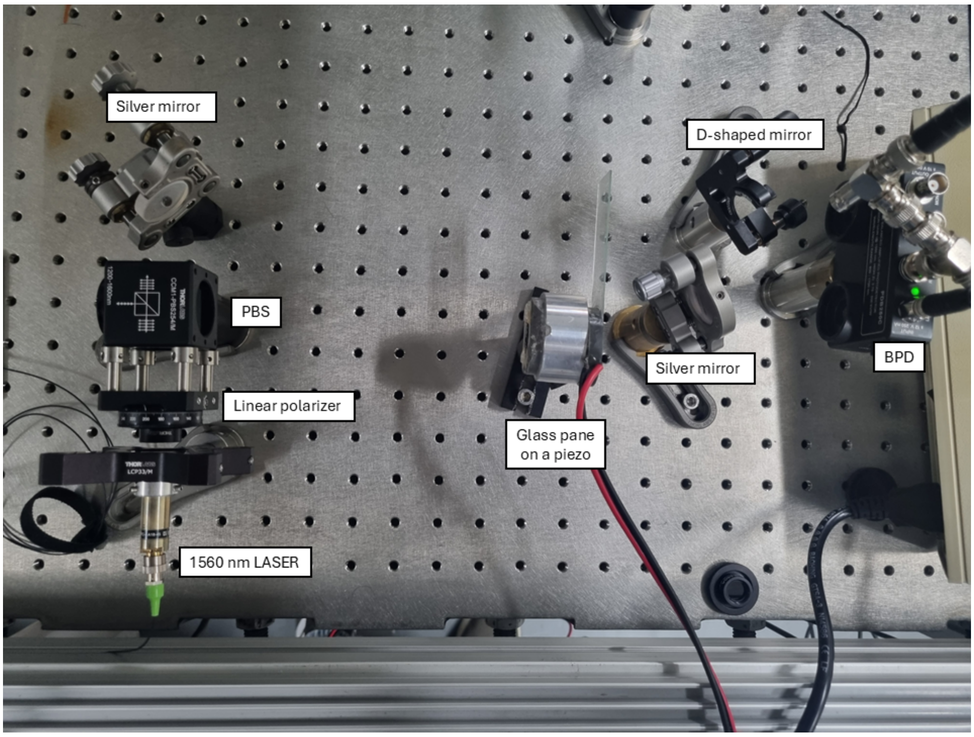

Figure 18: The setup of the secondary test experiment. The linear polarizer and PBS combination control the beam intensity to avoid saturation of the BPD. The detection system mimics that of the main experiment.

The 1560 nm beam is transmitted through the glass pane connected to the piezo. The beam is centered on the D shaped mirror so that each half of the beam reaches one of the photodiodes of the BPD. When the glass pane sits motionless, the signal on the BPD exhibits only small amplitude low frequency shifts, which are probably caused by physical vibrations of the optic components. The piezo is then given a sinusoidal electric potential to excite vibrations in the glass using a FG. In order to best observe the vibrations in the glass, the electric potential frequency must match the glass’s natural resonance frequency. To find the first mode of resonance, we simply tapped the glass and read the frequency of the BPD signal, 188 Hz. To find the next mode, we performed a manual frequency sweep until the next value that excited notable oscillations in the BPD signal, around 1168 Hz and 6275 Hz. We chose to work with 1168 Hz since it is the closest to the expected frequencies we will work with in the main experiment.

The signal from the BPD is then sampled by the RP, which performs IQ modulation. The modulated signal is then returned as a second input to the HV amplifier, summed with the FG signal and fed into the piezo.

Using the IQ cooling method, we managed to cool the motion of the glass by nearly 2 orders of magnitude. Results can be seen in Fig. 19.

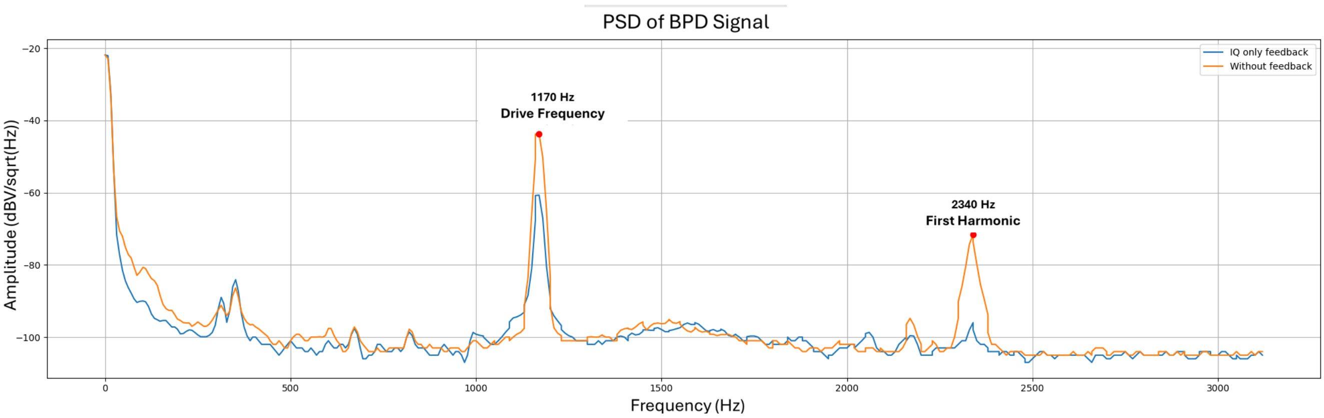

Figure 19: PSD of the BPD signal. Both with and without the IQ modulation cooling signal. In addition to the driving frequency peak at 1170 Hz, we can also observe the first harmonic at twice the driving frequency being cooled.

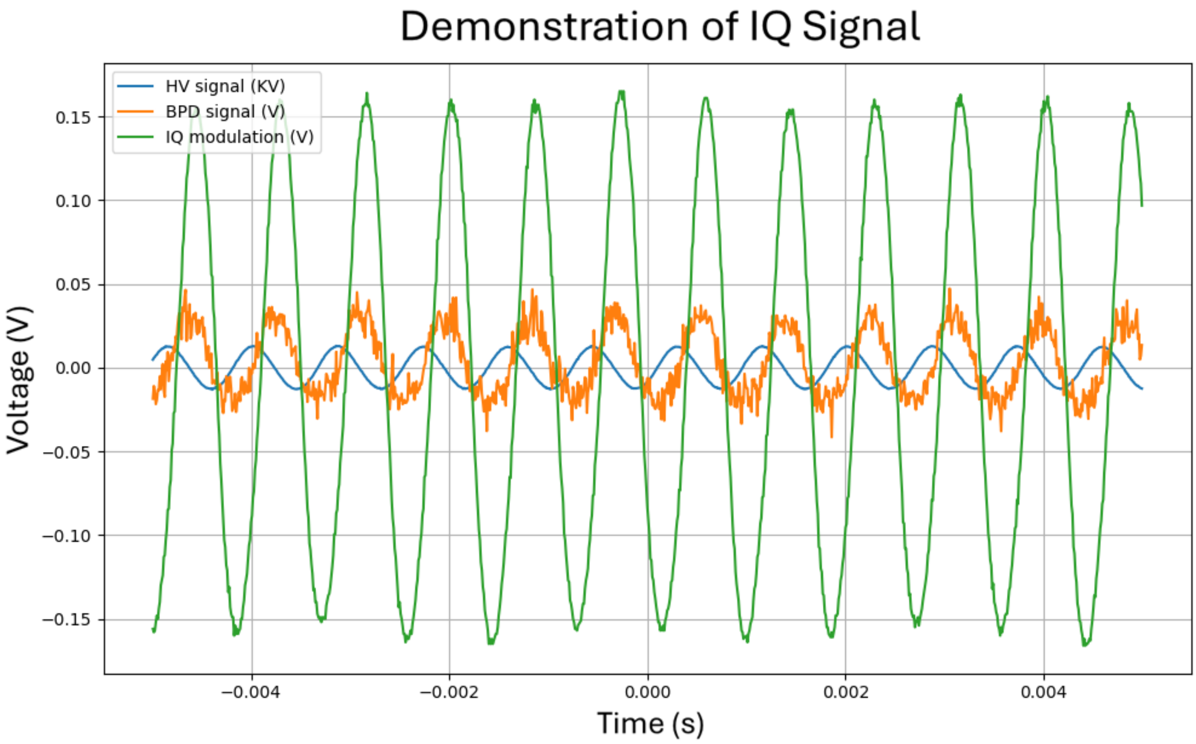

Figure 20: Scope reading of the piezo input, along with the BPD signal and the corresponding feedback given by the IQ module of the RP. The cooling signal from the IQ modulation is simply a smoothed and phase shifted position signal.

References

[1] O. Feldman, B. B. Shultz, M. Muretova, O. Dobkowski, Y. Japha, D. Grosswasser, and R. Folman, "Trapping and cooling of nanodiamonds in a Paul trap under ultra-high vacuum: Towards matter-wave interferometry with massive objects," arXiv:2508.14687 (2025).

[2] Y. Margalit, O. Dobkowski, Z. Zhou, O. Amit, Y. Japha, S. Moukouri, D. Rohrlich, A. Mazumdar, S. Bose, C. Henkel, and R. Folman, "Realization of a complete Stern-Gerlach interferometer: Towards a test of quantum gravity," *Science Advances* **7**, eabg2879 (2021).

[3] O. Dobkowski, B. Trok, P. Skakunenko, Y. Japha, D. Groswasser, M. Efremov, C. Marletto, I. Fuentes, R. Penrose, V. Vedral, W. P. Schleich, and R. Folman, "Observation of quantum free fall and the consistency with the equivalence principle," arXiv:2502.14535 (2025).

[4] S. Pedalino, B. E. Ramírez-Galindo, R. Ferstl, K. Hornberger, M. Arndt, and S. Gerlich, "Probing quantum mechanics with nanoparticle matter-wave interferometry," *Nature* **649**, 866 (2026).

[5] Q. Xiang, S. G. Elahi, A. Geraci, S. Bose, and A. Mazumdar, "Magnetic levitation and spatial superposition of a nanodiamond with a current-carrying chip," arXiv:2601.06608 (2026).

[6] C. Gonzalez-Ballestero, M. Aspelmeyer, L. Novotny, R. Quidant, and O. Romero-Isart, "Levitodynamics: Levitation and control of microscopic objects in vacuum," *Science* **374**, eabg3027 (2021).

[7] A. Ashkin, J. M. Dziedzic, J. E. Bjorkholm, and S. Chu, "Observation of a single-beam gradient force optical trap for dielectric particles," *Optics Letters* **11**, 288 (1986).

[8] V. V. Nesvizhevsky, F. Nez, S. A. Vasiliev, E. Widmann, P. Crivelli, S. Reynaud, and A. Y. Voronin, "A magneto-gravitational trap for precision studies of gravitational quantum states," *The European Physical Journal C* **80**, 520 (2020).

[9] N. Yu and W. Nagourney, "Analysis of Paul–Straubel trap and its variations," *Journal of Applied Physics* **77**, 3623 (1995).

[10] A. Pontin, H. Fu, M. Toroš, T. S. Monteiro, and P. F. Barker, "Simultaneous cooling of all six degrees of freedom of an optically levitated nanoparticle by elliptic coherent scattering," *Nature Physics* **19**, 1003 (2023).

[11] J. Gieseler, B. Deutsch, R. Quidant, and L. Novotny, "Subkelvin Parametric Feedback Cooling of a Laser-Trapped Nanoparticle," *Physical Review Letters* **109**, 103603 (2012).

[12] F. Tebbenjohanns, M. L. Mattana, M. Rossi, M. Frimmer, and L. Novotny, "Quantum control of a nanoparticle optically levitated in cryogenic free space," *Nature* **595**, 378 (2021).

[13] L. Magrini, P. Rosenzweig, C. Bach, A. Deutschmann-Olek, S. G. Hofer, S. Hong, N. Kiesel, A. Kugi, and M. Aspelmeyer, "Real-time optimal quantum control of mechanical motion at room temperature," *Nature* **595**, 373 (2021).

[14] J.-F. Hsu, P. Ji, C. W. Lewandowski, and B. D'Urso, "Cooling the Motion of Diamond Nanocrystals in a Magneto-Gravitational Trap in High Vacuum," *Scientific Reports* **6**, 30125 (2016).

[15] W. Paul, "Electromagnetic traps for charged and neutral particles," *Reviews of Modern Physics* **62**, 531 (1990).

[16] F. G. Major, V. N. Gheorghe, and G. Werth, *The Paul Trap*, Springer, Berlin, Heidelberg (2005).

[17] F. G. Major, *Charged Particle Traps.* Vol. 37, Springer Series on Atomic, Optical, and Plasma Physics, Springer-Verlag, Berlin, Heidelberg (2005).

[18] R. E. March, "Quadrupole ion traps," *Mass Spectrometry Reviews* **28**, 961 (2009).

[19] C. A. Schrama, E. Peik, W. W. Smith, and H. Walther, "Novel miniature ion traps," *Optics Communications* **101**, 32 (1993).

[20] T. Lindvall, K. J. Hanhijärvi, T. Fordell, and A. E. Wallin, "High-Accuracy Determination of Paul-Trap Stability Parameters for Electric-Quadrupole-Shift Prediction," *Journal of Applied Physics* **132**, 124401 (2022).

[21] J. B. Fenn, M. Mann, C. K. Meng, S. F. Wong, and C. M. Whitehouse, "Electrospray ionization–principles and practice," *Mass Spectrometry Reviews* **9**, 37 (1990).

[22] D. S. Bykov, P. Mestres, L. Dania, L. Schmöger, and T. E. Northup, "Direct loading of nanoparticles under high vacuum into a Paul trap for levitodynamical experiments," *Applied Physics Letters* **115**, 034101 (2019).

[23] E. Weisman, C. K. Galla, C. Montoya, E. Alejandro, J. Lim, M. Beck, G. P. Winstone, A. Grinin, W. Eom, and A. A. Geraci, "An apparatus for in-vacuum loading of nanoparticles into an optical trap," *Review of Scientific Instruments* **93**, 115115 (2022).

[24] A. Dahlin, "ESI positive mode." (2015). URL: `https://commons.wikimedia.org/wiki/File:ESI_positive_mode_(21589986840).jpg`.

[25] F. Gittes and C. F. Schmidt, "Interference model for back-focal-plane displacement detection in optical tweezers," *Optics Letters* **23**, 7 (1998).

[26] L. Dania, D. S. Bykov, M. Knoll, P. Mestres, and T. E. Northup, "Optical and electrical feedback cooling of a silica nanoparticle levitated in a Paul trap," *Physical Review Research* **3**, 013018 (2021).

[27] D. S. Lemons and A. Gythiel, "On the Theory of Brownian Motion," *American Journal of Physics* **65**, 1079 (1997).

[28] N. P. Bullier, A. Pontin, and P. F. Barker, "Super-resolution imaging of a low frequency levitated oscillator," *Review of Scientific Instruments* **90**, 093201 (2019).

[29] T. W. Penny, A. Pontin, and P. F. Barker, "Performance and limits of feedback cooling methods for levitated oscillators: a direct comparison," *Physical Review A* **104**, 023502 (2021).

[30] M. Poggio, C. L. Degen, H. J. Mamin, and D. Rugar, "Feedback cooling of a cantilever's fundamental mode below 5 mK," *Physical Review Letters* **99**, 017201 (2007).

[31] Y. Pei, S. Biswas, D. S. Fussell, and K. Pingali, "An Elementary Introduction to Kalman Filtering," arXiv:1710.04055 (2019).

[32] A. Waxman, “Sensitive Magnetometry Based on NV Centers in Diamonds.” PhD thesis (2019).

[33] Y. Schlussel, “Study of Nitrogen-Vacancy Centers in Diamond.” PhD thesis (2017).

[34] L. Dania, K. Heidegger, D. S. Bykov, G. Cerchiari, G. Araneda, and T. E. Northup, “Position measurement of a levitated nanoparticle via interference with its mirror image,” *Physical Review Letters* **129**, 013601 (2022).

[35] A. C. Frangeskou, A. T. M. A. Rahman, L. Gines, S. Mandal, O. A. Williams, P. F. Barker, and G. W. Morley, “Optical levitation of high purity nanodiamonds in vacuum without heating,” *New Journal of Physics* **20**, 043016 (2018).

[36] P. Skakunenko, D. Folman, Y. Bar-Haim, and R. Folman, “Strong Confinement of a Nanodiamond in a Needle Paul Trap: Towards Matter-Wave Interferometry with Massive Objects,” arXiv:2508.14272 (2025).

[37] J. Liao, M. Jost, M. Schaffner, M. Magno, M. Korb, L. Benini, F. Tebbenjohanns, R. Reimann, V. Jain, M. Gross, A. Militaru, M. Frimmer, and L. Novotny, “FPGA Implementation of a Kalman-Based Motion Estimator for Levitated Nanoparticles,” *IEEE Transactions on Instrumentation and Measurement* **68**, 2374 (2019).

[38] G. P. Conangla, F. Ricci, M. T. Cuairan, A. W. Schell, N. Meyer, and R. Quidant, “Optimal Feedback Cooling of a Charged Levitated Nanoparticle with Adaptive Control,” *Physical Review Letters* **122**, 223602 (2019).

[39] Y. Jin, K. Shen, P. Ju, X. Gao, C. Zu, A. J. Grine, and T. Li, “Quantum control and Berry phase of electron spins in rotating levitated diamonds in high vacuum,” *Nature Communications* **15**, 5063 (2024).

קירור חשמלי של נאנו חלקיקים במלכודת פול

בן שולץ

תואר מוסמך במדעים

אוניברסיטת בן-גוריון בנגב

תשפ"ו

תקציר

תזה זו מציגה את הפיתוח והיישום של מערכת קירור מבוססת משוב חשמלי עבור ננו-חלקיקים לכודים במלכודת פאול, במטרה לקדם את הבקרה המדויקת בניסויי לויטו-דינמיקה (levitodynamics). במסגרת המחקר, נעשה שימוש במלכודת פאול מסוג end-cap, שתוכננה באופן ייעודי לכליאה יציבה של ננו-חלקיקים טעונים, בעוד שמשוב חשמלי שימש להאטת תנועתם ולקירורם. גילוי אופטי של תנועות החלקיק בזמן אמת ממומש באמצעות מערך התאבכות הומודיני של האור המפוזר קדימה, וגילוי הטרודיני של האור המפוזר אחורה. נבחנו שתי טכניקות משוב אקטיביות: שיכוך מהירות (velocity damping) ומשוב פרמטרי. שתי השיטות יושמו על גבי פלטפורמה מבוססת FPGA של Red Pitaya, על מנת לעמוד בדרישות המחמירות של משוב בעל השהיה נמוכה (low-latency). תוצאות הקירור המוצגות בעבודה זו הושגו באמצעות שתי הטכניקות. כמו כן, חשוב לציין שבעוד שהמחקר והיישום של הקירור באמצעות שיכוך מהירות בוצעו על ידי, תוצאות הקירור הטובות ביותר הושגו על ידי עמיתיי למעבדה בזמן ששהיתי בשירות מילואים. כפועל יוצא של עבודתנו, העלינו לאחרונה טיוטה מוקדמת (preprint) לארכיון [1].

המערכת הניסויית המתוארת בתזה זו היא פרי עבודתם של שני דוקטורנטים, פוסט-דוקטורנט ואנוכי. השתתפתי בתכנון ובניית מערכת המלכודת ובהרכבת מערכת הוואקום, אך המוקד העיקרי של עבודתי היה מערכת הקירור ותהליך מזעור תנועת המיקרו.

אוניברסיטת בן-גוריון בנגב

הפקולטה למדעי הטבע

המחלקה לפיזיקה

קירור חשמלי של נאנו חלקיקים במלכודת פול

חיבור לשם קבלת התואר מוסמך בפקולטה למדעי הטבע

בן שולץ

בהנחיית **פרופ. רון פולמן**

מרץ, 2026 **ניסן, תשפ"ו**